Superfog Formation: Laboratory Experiments and Model Development

Project ID: 09-1-04-5

Final Project Report

January, 2013

Prepared for:
Joint Fire Science Program

By

Dr. Marko Princevac, Dr. David Weise, Dr. Akula Venkatram, Dr. Gary Achtemeier, Dr. Shankar Mahalingam, Dr. Scott Goodrick, Mr. Christian Bartolome

Table of Contents

List of Tables

List of Figures

Abstract

Several major car pileups with fatalities have resulted as a consequence of the formation of a dense smoke cloud which reduces visibility to less than 3 meters. These conditions of low visibility are known as Superfog. Continuing from work done by Dr. Gary Achtemeier, theoretical, numerical and physical laboratory modeling and experiments have been conducted on the topic of Superfog. Thermodynamic condensation, droplet size distribution, liquid water content, visibility relations and boundary layer development were explored through numerical analysis. Laboratory measurements of smoldering smoke, Superfog formation, and smoke boundary layer growth have been conducted. Based on these laboratory experiments and modeling we conclude that conditions likely to form Superfog are: droplet sizes less than 1 μm, cloud condensation nuclei (CCN) concentrations of 10^5 per ccm, liquid water content (lwc) greater than 2 g kg^{-1}, ambient temperature less than 40^oF, ambient humidity greater than 80%, fuel moisture content greater than 40%, and wind velocities less than 1 m s^{-1}. A Superfog Analysis Model (SAM) has been developed to aid land managers by enabling them to quickly asses situations as favorable or unfavorable to the formation of Superfog. The purpose of this tool is to prevent the formation of Superfog over highways. This tool has been validated by laboratory experiments and has been successful in predicting previous superfog events. Experimental, numerical and theoretical details are presented in this report. User manual for SAM is given in Appendix B of the report.

Nomenclature

CCN	Cloud condensation nuclei
Cp	Specific heat capacity
CSAT3	sonic anemometer
d	*D*istance
fmc	Fuel moisture content
h	Height of Superfog
h_{fg}	Latent heat of vaporization for water
HMP45C	Temperature and humidity sensor
I_t	Intensity in presence of optical medium
I_0	Intensity measured in clean air
K	Eddy Diffusivity
k	Von Karman constant
L	Obukhov length
lwc	Liquid water content
PDPA	Phase Doppler Particle Analyzer
p_s	Saturation vapor pressure
Q_e	Extinction Efficiency
q_{mass}	Water vapor flux
q_{heat}	Heat flux
r	Droplet radius
RC01	Irradiative and convective heat flux sensor
T	Temperature
t	Time
u_*	Friction Velocity

Vis	Visibility
v	Water vapor
w	Mixing ratio
w_l	Excess liquid mixing ratio
w_{sat}	Saturation mixing ratio
z	Vertical height
z_0	Surface roughness length

Greek

β	Extinction coefficient
κ	Thermal diffusivity
λ	Wavelength of light
μ	Limit of contrast
ρ_a	Density of air
ρ_l	Density liquid water
σ	Geometric standard deviation
σ_w	Surface tension of water

1. Introduction

1.1 Superfog Occurrences

Visibility impairment caused by smoke from wild and prescribed fires passing over major roadways have lead to serious vehicular pile ups in the past years. Property loss or damage, loss of life, and millions of dollars on legal proceedings and liabilities have resulted. These extreme visibility impairments when visibility drops to under 3 m (10 ft) are referred as Superfog. One of the main properties of Superfog is its fast formation. Some Superfog examples follow.

In January 9, 2008 on the I-4 in Polk County a Superfog event resulting from a nearby prescribed fire caused a 70 car pileup which resulted in 5 fatalities and 38 injuries.

In 2011 wildfires caused low visibility events to occur closing numerous highways over the 3 months of burning and smoldering at the Great Dismal Swamp National Wildlife Refuge. There were isolated vehicular accidents caused by low visibility despite best efforts of highway management.

In December 2011 marsh wildfire smoke caused Superfog conditions leading to major a car pileup on the I-10 at New Orleans, LA. The accident caused 2 deaths and 61 injuries.

In January 2012 a Superfog event formed with smoke from a nearby wildfire on the I-75 near Gainesville, FL. The pileup included 7 semi-trucks and 12 cars. This tragic incident claimed 10 lives and left 21 injured.

1.2 Previous Research on Superfog

Superfog has been studied extensively by Dr. Achtemeier of the USDA FS (Achtemeier 2001, 2003, 2008 and 2009). His previous work has examined the effects of mono disperse droplet formation on the visibility with respect to size and number of droplets (Achtemeier 2009). He tabulated smoke temperature and humidity measurements for smoldering litters in the field (Achtemeier 2008). He used simple thermodynamic modeling to approximate condensation conditions (Achtemeier 2008). He has also worked on projects involving tracking smoke and fog travel in evening hours guided by drainage ditches (Achtemeier 2003).

Superfog is currently hypothesized to form during the smoldering phase of a wildland fire in the night hours. Due to its relatively lower heat output, the smoldering phase is more prone to Superfog formation and as such will be given major attention in this report in comparison to the flaming phase. There are two main ingredients that lead to the formation of Superfog from fire: water vapor and combustion particulates upon which water vapor condenses (Hallett et al. 2007). Water vapor results from a combination of products of combustion reaction, vaporization of water from live and dead fuels due to surface heating, and from ambient moisture of air (figure 2.1). Mixing between the cool ambient air, hot water vapor, and cloud condensation nuclei (CCN) will lead to condensation into droplets (Asa-Awuku et al 2009). Based on the

temperature and water content of the smoke source and ambient air entrained into the smoke, Superfog will either form or fail to occur as determined by the thermodynamics of the mixture (Achtemeier 2008). The presence of numerous droplets in air causes extreme light scattering, thereby reducing visibility (Tang 1996). Visibility is strongly dependent on the size distribution of particles and the number concentration of droplets. Empirical measurements of naturally occurring fog suggest that liquid water content values of 5 g m^{-3} are required to form Superfog (Elderidge 1971, Nebuloni 2005, Podzimek 1997).

1.3 Report Structure

The relevant theory is presented in Section 2. Section 2.1 introduces a thermodynamic model that predicts conditions for water vapor condensation when hot moist air resulting from fuel combustion mixes with ambient air. In Section 2.2 the relationships between visibility, liquid water content, droplet size distribution and concentration are examined. Section 2.3 presents Kohler theories associated with cloud condensation nuclei and growth of droplets. Section 2.4 outlines a two dimensional boundary layer dispersion model to simulate the formation of smoke. Experimental measurement tools and analysis are described in section 3. Section 3.1 focuses on the small fog chamber experiments and PDPA measurements of size distribution and number concentration. Section 3.2 presents the wind tunnel and climate control modifications. Items within section 3.3 describe instrumentation and measurement methods. In Section 3.4 t Smoke Measurements in non-air-conditioned wind tunnel and small, circular, fuel bed are presented. Section 3.4 presents results from Superfog Formation Experiments within the air-conditioned wind tunnel. Section 3.5 presents the model and experiment comparison. Section 4 presents 2D boundary layer model's ability to predict historic Superfog events. Section 5 summarizes key points, major achievements and recommendations as an outcome of the completed project effort.

2. Theory

The two main ingredients from a smoldering phase of a prescribed burn that contribute to Superfog events are water vapor and particulates. Water vapor that arises from combustion of fuel and surface heating of moist soil condenses onto smoke particulates in the cooler atmosphere. This condensation can be enhanced if the ambient air is also humid. The droplets, which are the result of condensation on smoke particles, scatter light thus decreasing visibility. The main Superfog ingredients are schematically presented in Figure 2.1. This decrease in visibility results in a higher probability of motor vehicle related accidents in areas where smoke and fog cross over highways.

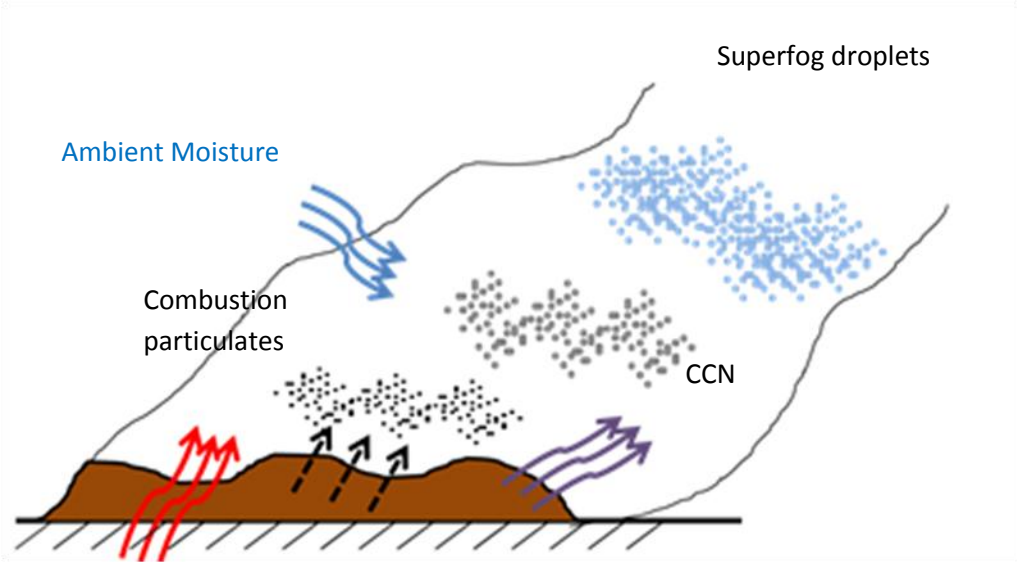

Figure 2.1. Main Superfog ingredients. Moisture is released as a product of combustion, and water evaporation from fuels and soil. Particles that result from combustion readily became Cloud Condensation Nuclei (CCN). Water vapor from fire and ambient condenses on newly formed CCN leading to Superfog.

2.1 Thermodynamic model

The first step in improving our understanding of Superfog, was to clarify the underlying thermodynamics as delineated by Achtemeier (2008). The basis of the Achtemeier's model is presented in figure 2.2. The model considered a mixture of hot air and smoke from fire, with colder ambient air.

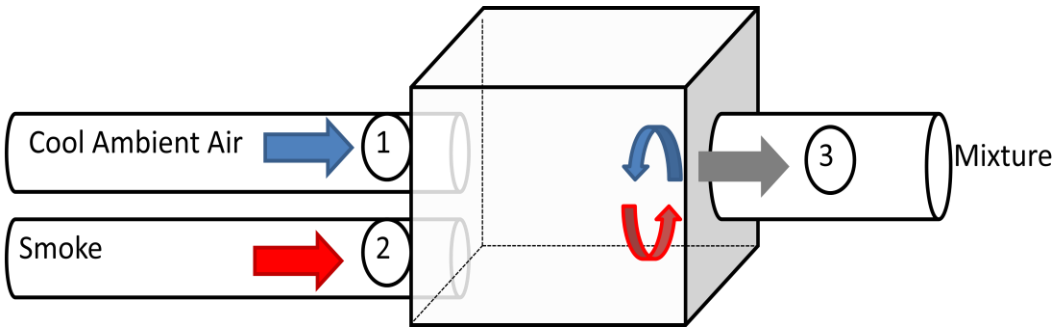

Figure 2.2. A simple thermodynamics model considers a mixture of cold ambient air with hot air with smoke resulting from the fire.

The conservation of mixing ratio for the system in Figure 2.2. is

$$m_1 w_1 + m_2 w_2 = m_3 w_3 \tag{2.1}$$

where *m* indicates the mass of air and *w* indicates the mixing ratio. Subscripts 1, 2 and 3 refer to ambient air, hot air above the fire (smoke) and mixture, respectively. The mixing ratio is a measure of water vapor mass and is commonly given as water vapor concentration in grams of water vapor per kilogram of dry air.

The energy equation for cases where water vapor condenses can be written as

$$m_1 T_1 + m_2 T_2 = m_3 T_3 + dT = T_f \tag{2.2}$$

where T_1 and T_2 are the temperatures of the ambient and smoke conditions respectively, dT is the temperature change due to latent energy released during condensation, and T_f is the final mixture temperature. The quantity T_3 is an initial weighted average estimate of the mixture temperature calculated as

$$T_3 = \frac{m_1 T_1 + m_2 T_2}{m_1 + m_2} \tag{2.3}$$

The change in temperature dT due to the released latent energy is calculated as

$$dT = \left(w_3 - w_{sat}\right)\frac{h_{fg}}{C_p} \tag{2.4}$$

where w_{sat} is the saturation mixing ratio, h_{fg} is the latent heat of vaporization for water, and C_p is the specific heat capacity of water. It is important to note that the saturation mixing ratio is a nonlinear function of temperature. The conservation equations were cast in a form suitable for iterative solution as:

$$f\left(T_f\right) = T_f - T_3 - \left(w_3 - w_{sat}\right)\frac{h_{fg}}{C_p} = 0 \tag{2.5}$$

Noting that the latent energy and heat capacity do not depend on temperature the derivative function was obtained

$$f'\left(T_f\right) = 1 + \frac{h_{fg}}{C_p}\frac{d}{dT}\left(w_{sat}\right) \tag{2.7}$$

For the dependence of the vapor pressure of water as a function of temperature we adopted Lowe's (1976) polynomial function given as

$$p_s(T) = a_0 + a_1 T + a_2 T^2 + a_3 T^3 + a_4 T^4 + a_5 T^5 + a_6 T^6 \tag{2.8}$$

Here p_s is the saturation vapor pressure in millibars, T is the temperature in degrees Celsius, and a_0-a_6 are experimentally determined fit coefficients given in Table 2.1.

Table 2.1. Lowe's coefficients for polynomial dependence of saturation vapor pressure in with temperature (Equation 2.8).

Coefficient	Value
a_0	6.107799961
a_1	4.436518521e-1
a_2	1.428945805e-2
a_3	2.650648471e-4
a_4	3.031240396e-6
a_5	2.034080948e-8
a_6	6.136820929e-11

The saturation vapor pressure, p_s, is converted to the saturation mixing ratio w_{sat} as

$$w_{sat} = \frac{.622 \cdot p_s}{1013.25 - p_s} \cdot 1000 \tag{2.9}$$

In this form, the saturation mixing ratio has units of grams of water vapor per kilogram of dry air.

Using the Newton Raphson method the iterative equation can be written as

$$T_f^{i+1} = T_f^i - \frac{f\left(T_f^i\right)}{f'\left(T_f^i\right)} \tag{2.10}$$

The excess mixing ratio is expressed as

$$w_l = w_3 - w_s(T_f) \tag{2.11}$$

where w_l is the excess liquid mixing ratio and $w_s(T_f)$ is the saturation mixing ratio at the final mixture temperature. The excess liquid mixing ratio can be related to the liquid water content as

$$LWC = w_l \rho_a \tag{2.12}$$

where ρ_a is the density of air.

Table 2.2 summarizes comparisons between the thermodynamic models with and without consideration of latent heat when measured conditions (Achtemeier, 2008) are used as the input.

Table 2.2. Final mixture temperature and liquid water content predicted by two models, with and without incorporation of latent heat. Measured smoke temperatures and mixing ratios from Achtemeier 2009.

Measured Conditions – Model Input				Model Without Latent Heat Consideration		Model With Latent Heat Consideration	
T_1 [C]	w_1 [g/kg]	T_2 [C]	w_2 [g/kg]	Final Mixture Temperature [^{o}C]	Final Mixture *LWC* [g m^{-3}]	Final Mixture Temperature [^{o}C]	Final Mixture *LWC* [g m^{-3}]
34.8	34.69	15	6.2	24.9	1.24	25.15	0
42.1	51.98	15	6.2	28.6	5.28	30.45	0.92
41.2	47.2	15	6.2	28.1	3.51	29.20	0.53
46.4	61.65	15	6.2	30.7	6.99	33.02	1.11
40.3	46.7	15	6.2	27.7	3.86	28.98	0.65
54.1	93.9	15	6.2	34.6	16.6	39.46	2.31
45.8	60.1	15	6.2	30.4	6.67	32.63	1.07
62.5	134.34	15	6.2	38.8	28.19	45.42	3.08

Results in table 2.2 indicate that with the inclusion of latent heat, energy balance predicts significantly different liquid water content available for fog formation. Based on empirical models (Fisak, 2006) a *LWC* of 2.2 [g m^{-3}] was reported to be sufficient to produce Superfog (*Vis*<3m). The model result from table 2.2 indicate that achieving *LWC* values up to 2.2 [g m^{-3}] can be difficult and the actual *LWC* may be insufficient to produce Superfog visibilities. Thus, the next logical step was to examine the role of particulates on the Superfog formation process.

2.2. Relationship of *LWC* and Visibility

A sensitivity test was conducted to investigate the impact of different distributions of droplet sizes on final visibilities. For this purpose, the liquid water content was calculated as

$$LWC = \sum n_i \frac{4\pi}{3} r_i^3 \rho_l \tag{2.13}$$

where r_i is the radius of particle, n_i is the number density of particles of size r_i, and ρ_l is the density of water.

The visibility is related to the extinction coefficient β, via (Achtemeier 2008)

$$Vis = -\frac{\ln(0.02)}{\beta} \tag{2.14}$$

Here the limit of contrast is expressed as the constant 0.02. The extinction coefficient is calculated as

$$\beta = \sum \pi Q_e(r_i, \lambda) n_i r_i^2 \tag{2.15}$$

where Q_e is the extinction efficiency (calculated via Mie theory as function of both size r_i, and wavelength of light l). In Figure 2.3 a plot of the extinction efficiency is presented for four wavelengths. We see that droplets with radii less than 1 micrometer can have extinction efficiencies near 4, compared to the larger particles of extinction efficiency 2. For droplets with radii larger than 2 micrometers, the extinction efficiency oscillates around a value of 2.

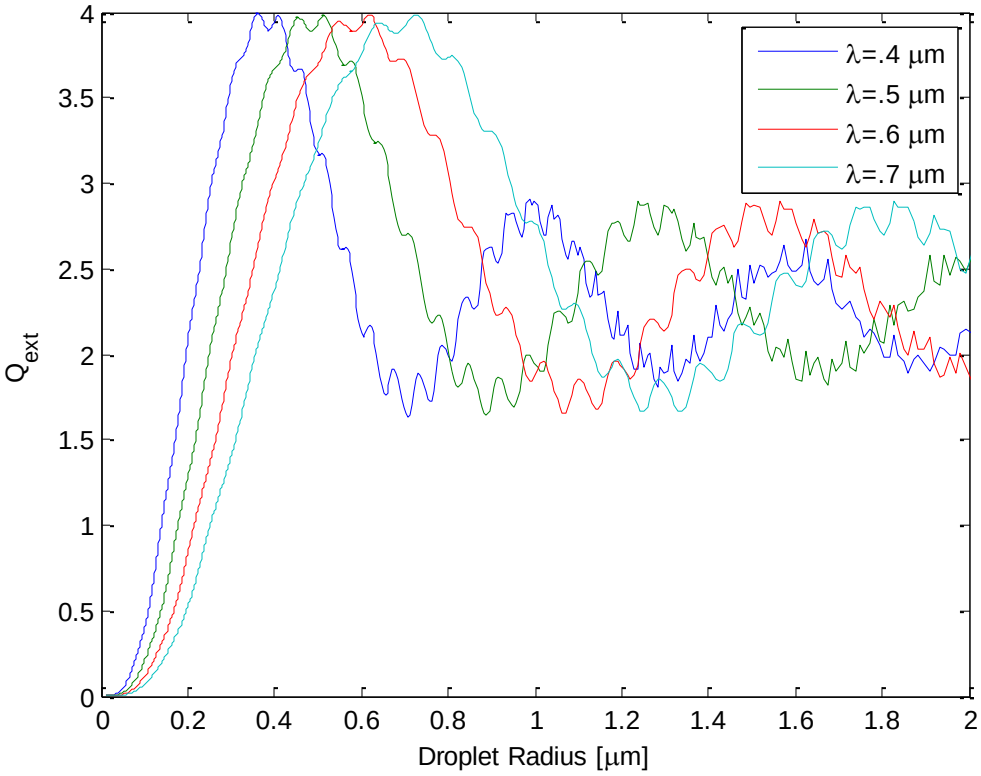

Figure 2.3. The extinction efficiency for four wavelengths of light as a function of water droplet radius.

We see that both liquid water content and visibility are strongly dependent on the size distribution and number concentrations of the droplets formed. For a lognormal droplet size distribution (Podzimek, 1997) the distribution of droplet sizes can be expressed as

$$n(r) = \frac{n_{total}}{\sqrt{2\pi}\ln\sigma}\exp\left[\frac{-\left(\ln\frac{r}{r_g}\right)^2}{2(\ln\sigma)^2}\right] \tag{2.16}$$

Thus the liquid water content, and extinction coefficient β, can be expressed in the following integral forms:

$$LWC = \int_{r_1}^{r_2} \frac{4\pi}{3} r^3 \rho_l\, n(r) dr \tag{2.17}$$

where r is the radius of particle, r_1 is the smallest droplet size limit, r_2 is the largest droplet size limit, $n(r)$ is the probability density function for the droplet size distribution, and ρ_l is the density of water. The extinction coefficient (Nebuloni, 2005) is calculated as

$$\beta = \int_{r_1}^{r_2} \pi Q_e(r,\lambda) n(r) r^2 dr \tag{2.18}$$

All integrals were evaluated using ten-point gauss quadrature. Numerical experiments were conducted for the parameter ranges given in Table 2.3.

Table 2.3. Parameter ranges covered in numerical tests to determine the sensitivity of visibility to droplet size, standard deviation of size distribution, CCN concentration and LWC.

Parameter	Range
Visibility	3, 5 and 10 [m]
LWC	0 – 12 [g m^{-3}]
Droplet Radius	1 – 10 [μm]
CCN Concentration	10^2 - 10^7 [# cm^{-3}]

With the known available liquid water content from thermodynamic analysis (Table 2.2) and desired visibility of 3m for Superfog ,a sensitivity study was conducted on the relationship between equations 2.14, 2.16, 2.17 and 2.18. To satisfy these coupled equations various lognormal size distributions for the droplet aerosols were investigated. Results from these analyses are presented in figure 2.4.

Relationships between the liquid water content and the geometric radius for three iso-visibilities are presented in figure 2.4a. For the desired Superfog visibility and known available liquid water content (2 g m^{-3}) the relation suggests that the droplet size distribution should have a geometric mean radius of 1 μm or less.

The number density of droplet aerosols vs. mean geometric radius was also investigated (figure 2.4b) for different visibilities. Assuming the droplet size distribution to have a geometric radius of 1μm or less, then the number density for the fog should be of the order of 10^5 or greater [# cm^{-3}].

For a set visibility, the influence of distribution spread on required liquid water content and number density was investigated (figure 2.4c). It can be seen from the plot that an increase of spread dramatically increases the liquid water content necessary for Superfog formation by including larger diameter particles. For viable *LWC* values and distributions with mean geometric radius less than 1 μm the size distribution spread could not be larger than σ=1.3.

From the figure 2.4d we can see that for droplet distributions centered at about 6 μm or greater do not seem to play a major role in the number of droplets formed. However at smaller sizes, the number density necessary for Superfog formation σ values plays a greater role. Distributions with greater spread are able to form Superfog with fewer droplets. However since *LWC* available is a limiting factor the σ value for feasible liquid water contents is 1.3 and droplet number concentrations should be 7.5 x 10^5 per ccm.

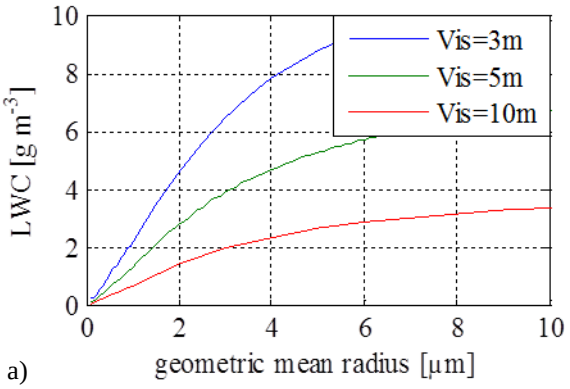

a)

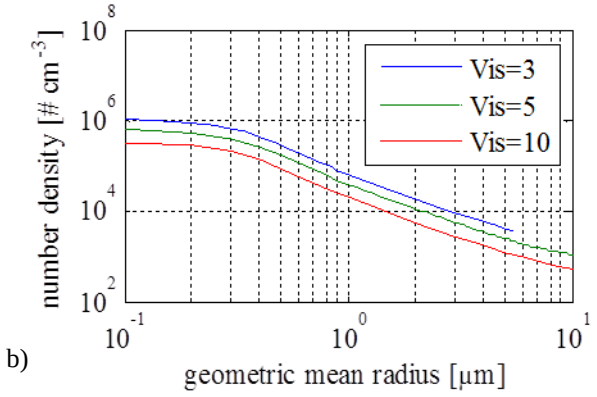

b)

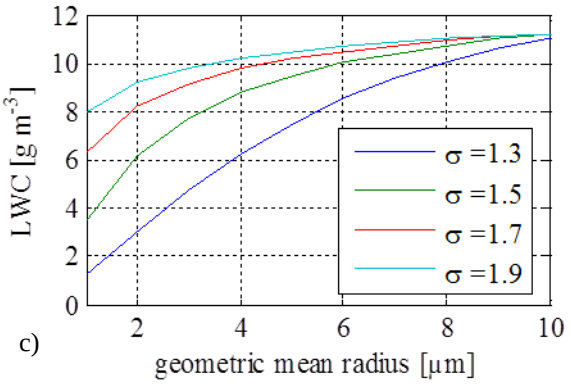

c)

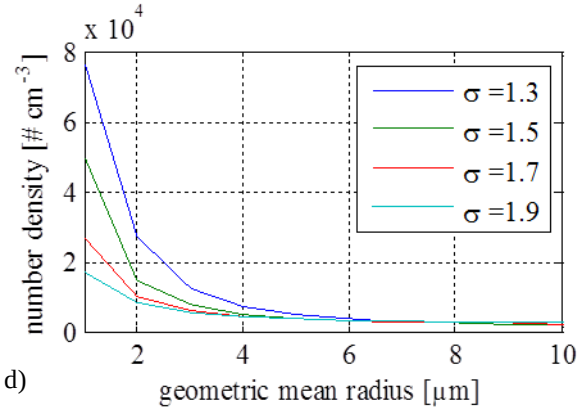

d)

Figure 2.4. Results of visibility, *LWC*, and droplet size distribution sensitivity study. Relationship between *LWC* and geometric mean radius for iso-visibilities of 3, 5 and 10 meters (a). Relationship between number density of droplets and particle radius for iso-visibilities of 3, 5 and 10 meters (b). *LWC* vs mean geometric radius for visibility set to 3 meters and distribution spread, σ, ranging from 1.3 to 1.9 (c). Droplet number concentration against mean geometric radius for visibility set to 3 meters and distribution spread, σ, ranging from 1.3 to 1.9 (d).

Based on this sensitivity study it is concluded that the number of CCN and droplet size distribution are key components to the formation of Superfog for reasonable (realistic, achievable in the field) liquid water contents (LWC<2 [g cm^{-3}]). To achieve this, it is important to have size distributions with geometric mean radius less than or equal to 1μm. We also see that the number of particles necessary to have extremely low visibilities and low *LWC*s is in the order of millions of particles per cubic centimeter. Estimates of Holle (1971) and Egan et al. (1974) suggest that CCN produced by a gram of wood fuel is capable of producing 6×10^{10} particulates per gram of fuel consumed, thus over satisfying needs suggested by the sensitivity study.

Podzimek (1997) measurement and experimental measurements later to be presented of fog without the presence of combustion CCN have modal droplet sizes larger than sensitivity study suggests. It is this reason the presence of high concentrations of CCN are crucial to the formation of Superfog. In the next section a study of Kohler theory and CCN impact on droplet growth.

2.3. Kohler theory

To this point, the effects of cloud condensation nuclei (CCN) on water condensation have not been considered. In the current formulation, relative humidity will need to exceed 100% for small droplets to form without the presence of particles. However, CCN particles attract water vapor and dissolve to form a droplet solution thus decreasing the saturation vapor pressure as explained by the Kelvin equation (Seinfeld and Pandis, 2006)

$$S = \frac{p_w(D_p)}{p_w^{sat}} = x_w \gamma_w \exp\left(\frac{4\upsilon_w \sigma_w}{RTD_p}\right) \tag{2.19}$$

where S is the saturation ratio, $p_w(D_p)$ is the partial pressure of the water vapor at the surface of the droplet, p_w^{sat} is the saturation partial pressure of the water vapor in the surrounding environment, x_w is the mole fraction of water in the solution droplet, γ_w is the water activity coefficient, σ_w is the surface tension of water, D_p is diameter of droplet, R is the ideal gas constant, T is the temperature and ϖ, υ_ω is the molar volume of the droplet. Common interpretation of the Kelvin equation for cloud droplets uses assumptions such as dilute solution and water activity coefficient equal to 1 to formulate the Kohler equation. Using the procedure used in the text (Sienfeld and Pandis, 2006) a modification of the Kelvin equation without implementing these unfit assumptions for high concentrations possible in pyro-cumulus clouds is presented as

$$\ln\left(\frac{p_w(D_p)}{p_o}\right) = \ln(RH) = \frac{4\upsilon_w\sigma_w}{RTD_p} + \ln\gamma_w - \ln\left(1 + \frac{v_s n_s \upsilon_w}{\frac{\pi}{6}D_p^3 - v_s n_s \upsilon_w}\right) \tag{2.20}$$

where v_s is the van't-Hoff factor, n_s is the moles of solute. Eq. 2.20 shows the changes in the relative humidity, *RH*, needed to form a droplet where the first term represents the effect of the surface tension, the second term accounts for the water activity coefficient of the solute, and the last term accounts for the solute concentration. The available solute serves as CCN. To relate the molar solute concentration to the measurable fire emission concentration for the third term (Eq. 2.20) may be represented as

$$n_s = \frac{C_s}{\#\text{CCN}}\frac{1}{M_s} \tag{2.21}$$

where #CCN is the number density of droplets, C_s is the solute concentration and M_s is the molar mass of the solute.

The equations presented above form the framework for establishing relationship between visibility reductions, smoke and environmental conditions.

However, the presented framework has numerous uncertainties, including the droplet size distribution, homogenous or inhomogeneous growth of droplets and water vapor balance between droplet population and environment. At this time no further progress was made. This can be an area of further research.

2.4. 2D Boundary Layer Model

To properly understand Superfog formation it is necessary to look into the development of a boundary layer based model. For this reason expanding the thermodynamic model and including it within an appropriate boundary layer model was the next step considered. The advection diffusion equation is the base of our model and in its differential form is expressed as

$$\frac{\partial\phi}{\partial t} + u\frac{\partial\phi}{\partial x} = \frac{\partial}{\partial z}K\frac{\partial\phi}{\partial z} \tag{2.22}$$

where ϕ is any transported property in 2D space where x is the downwind direction and z is the vertical direction, *t* is time and *K* is the eddy diffusivity. The velocity profile, *u*, is expressed as a logarithmic profile (Cimorelli et al. 2005)

$$u(z) = \frac{u_*}{k}\left[\ln\left(\frac{z}{z_0}\right) + 4.7\frac{z}{L}\right] \tag{2.23}$$

where u_* is the friction velocity, *k* is the Von Karman constant, z_0 is the roughness length, and *L* is the Obukhov length. Here we focus on the transport equations of Temperature, *T*, water vapor *v*, and *LWC*.

$$\frac{\partial T}{\partial t} + u\frac{\partial T}{\partial x} = \frac{\partial}{\partial z}K\frac{\partial T}{dz} \tag{2.24}$$

$$\frac{\partial v}{\partial t} + u\frac{\partial v}{\partial x} = \frac{\partial}{\partial z}K\frac{\partial v}{\partial z} \tag{2.25}$$

$$\frac{\partial LWC}{\partial t} + u\frac{\partial LWC}{\partial x} = \frac{\partial}{\partial z}K\frac{\partial LWC}{\partial z} \tag{2.26}$$

The advection diffusion equations are solved by using an implicit finite difference method expressed in terms of a generic transport variable ϕ as

$$\frac{\phi_{i,j}^{n+1}\phi_{i,j}^{n}}{\Delta t} = u_{i,j}\frac{\phi_{i,j}^{n+1} - \phi_{i\text{-}1,j}^{n+1}}{\Delta x} = \frac{2}{z_{j+1} - z_{j-1}}\left(k_{j+\frac{1}{2}}\frac{\phi_{i,j+1}^{n+1} - \phi_{i,j}^{n+1}}{z_{j+1} - z_{j}} - k_{j-\frac{1}{2}}\frac{\phi_{i,j}^{n+1} - \phi_{i,j\text{-}1}^{n+1}}{z_{j} - z_{j-1}}\right) \tag{2.27}$$

where the subscript i indicates a downstream grid point, subscript j indicates a position of vertical grid point, superscript n indicates an iterative count, u is the downstream velocity, and k is the eddy diffusivity. A simple representation of points of interest of the finite difference equation is given in figure 2.

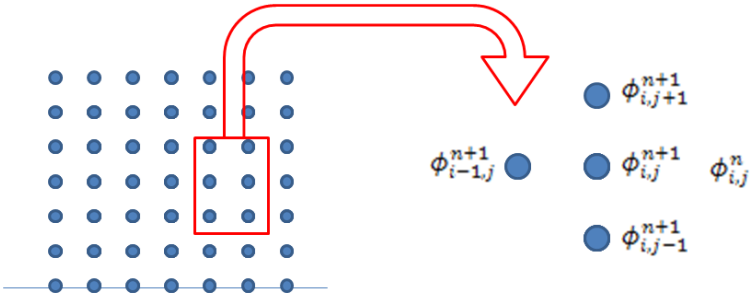

Figure 2.5. Numerical Node point location

The finite element equation was further simplified to the form

$$\phi_{i.,j}^{n+1} - \phi_{i.,j}^{n} + \beta\left(\phi_{i.,j}^{n+1} - \phi_{i-1.,j}^{n}\right) = \alpha_{j+\frac{1}{2}}\left(\phi_{i.,j+1}^{n+1} - \phi_{i.,j}^{n+1}\right) - \alpha_{j-\frac{1}{2}}\left(\phi_{i.,j}^{n+1} - \phi_{i.,j-1}^{n+1}\right) \tag{2.28}$$

where the quantities α and β are defined as

$$\beta = \frac{u_{i,j}\Delta t}{\Delta x} \tag{2.29}$$

$$\alpha_{j+\frac{1}{2}} = \frac{2k_{j+\frac{1}{2}}\Delta t}{\left(z_{j+1} - z_{j-1}\right)\left(z_{j+1} - z_{j}\right)} \tag{2.30}$$

$$\alpha_{j-1/2} = -\frac{2k_{j-1/2}\Delta t}{(z_{j+1} - z_{j-1})(z_j - z_{j-1})} \tag{2.31}$$

The finite difference equation is further simplified and solved using a tri-diagonal matrix solver. The discretized equation is:

$$a_j \phi_{i,j-1}^{n+1} + b_j \phi_{i,j}^{n+1} + c_j \phi_{i,j+1}^{n+1} = \phi_{i,j}^{n} + \phi_{i-1,j}^{n+1} \tag{2.32}$$

The coefficients a_j, b_j, and c_j are defined as

$$a_j = -\alpha_{j-1/2} \tag{2.33}$$

$$b_j = -\alpha_{j+1/2} \tag{2.34}$$

$$c_j = 1 + \beta + \alpha_{j-1/2} + \alpha_{j+1/2} \tag{2.35}$$

Now the method to solve the differential equation is essentially well formulated, and we require boundary conditions to solve the problem. The first boundary condition is a zero flux at the top of the boundary layer where the inversion layer prevents further transport in the vertical direction. The second boundary condition is a constant flux of heat and vapor from the ground level where smoldering fuels contribute. We assume that the heat and vapor flux is evenly distributed throughout the downwind distance of the model.

Constant heat flux from ground surface

$$q_{mass} = K\frac{\Delta v}{\Delta z} \tag{2.36}$$

Where v is the vapor concentration

$$q_{heat} = \rho C_p K\frac{\Delta T}{\Delta z} \tag{2.37}$$

$$K = \frac{\kappa}{\rho C_p} \tag{2.38}$$

Here κ is the thermal diffusivity and K is the eddy diffusivity. This system of equations is the structure of our Superfog modeling tool. The necessary inputs for this model are: vapor and heat flux, surface temperature, temperature gradient, relative humidity, friction velocity, Obukhov length, and roughness length.

2.5. Water Vapor Flux Approximation

The water vapor produced from smoldering fuel bed was approximated using stoichiometry. The approximate hydrocarbon for wood fuels can be expressed as $C_6H_9O_4$ (Ward 2001 and Parmar 2008). The balanced combustion equation for this hydrocarbon is

$$4C_6H_9O_5 + 25O_2 \Rightarrow 24CO_2 + 18H_2O \tag{2.39}$$

The mass of the hydrocarbon is estimated by

$$m_{hydrocarbon} = (1 - fmc) \cdot m_{fuel} \tag{2.40}$$

Where $m_{hydrocarbon}$ is the mass of $C_6H_9O_4$ available, *fmc* is the fuel moisture content, and m_{fuel} is the mass of the biomass fuel. The mass of $C_6H_9O_4$ is converted to moles and substituted into eq. 2.39 to find the moles of H_20 vapor formed. Assuming all fuel moisture evaporated, the water vapor produced from the combustion of the fuel bed can be expressed as

$$v_{total} = v_{combustion} + v_{fmc} \tag{2.41}$$

where $v_{combustion}$ is the mass of water vapor produced from combustion, v_{fmc} is the mass of evaporated water from the *fmc*, and v_{total} is the combined mass of water vapor produced from fuel bed. Figure 2.6 plots the estimations water vapor produced by the fuel bed after combustion normalized by fuel bed mass. From this analysis we can see that if a dry fuel without having no *fmc*, then the water vapor produced from combustion alone will be slightly above 50% of the original fuel bed mass. We also can see that the addition of *fmc* increases the total water vapor being produced. The contributions from combustion and evaporated *fmc* are balanced just above 35% *fmc*.

In experiments described in smoke measurements and superfog formation experiments 400 gram fuel beds were used in a cylindrical wire mesh. The diameter of the mesh container is approximately 0.33 meters, having area of 0.07 m^{-2}. The 400g fuel bed can produce 220 to 310 g of water vapor depending of fuel moisture content contributions. In general fuel beds in the experiments conducted smoldered for approximately 30 minutes. In the measurements using the wire mesh container the smoldering fuel bed produces water vapor flux is approximated to be 1.6-2.4 g m^{-2} s^{-1}. The water vapor flux approximations were used in the 2D boundary layer model.

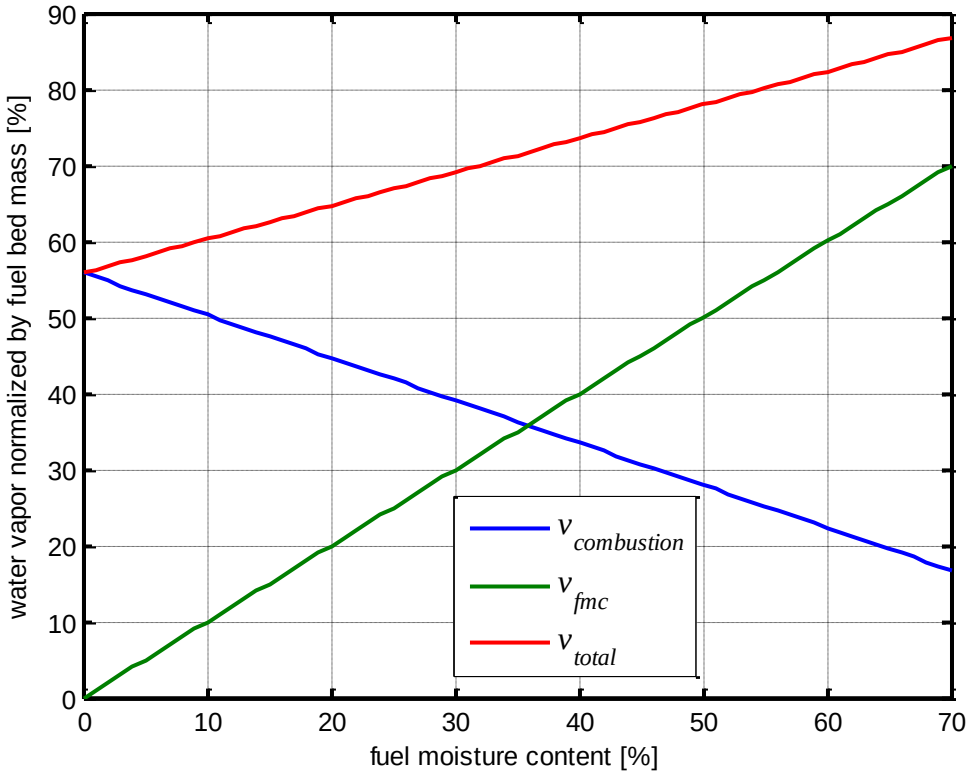

Figure 2.6. The total water vapor production from combustion and fuel moisture evaporation as a function of the fuel moisture content.

3. Experiments

3.1 Small Fog Chamber

3.1.1. Small Fog Chamber Description

The theoretical and numerical modeling presented in Section 2 delineated the sensitivity of fog formation on several parameters. Guided by these results we decided to first design a small and simple setup for initial tests before investing in modifications of the existing large wind tunnel. A number of experiments were conducted in a small acrylic chamber to test the viability of Superfog formation. The test chamber was designed based on the thermodynamic model schematic in Figure 2.2. with the addition of a fuel bed and a humidifier as presented in a schematic in Figure 3.1.

Rather than immediately proceed to modifications of the large wind tunnel, this simpler experimental setup, was made first to get a feel for controls range and precision necessary to produce fog and the various measurements of numerous properties associated with formation of fog and visibility.

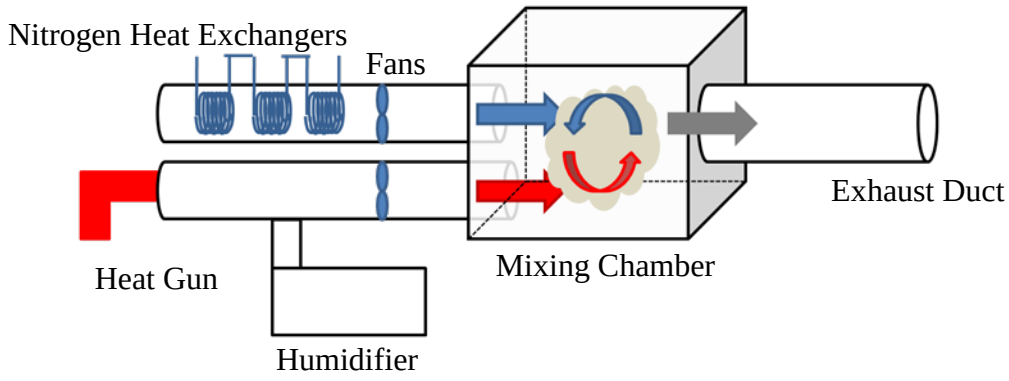

Figure 3.1. Schematic of Superfog box chamber

As described in Section 2, cool air, water vapor and particles from smoldering combine to produce low visibility smoke and fog. Based on a schematic in Figure 3.1, a 2 ft × 2 ft × 3ft optically clear acrylic chamber was built (Figure 3.2). This is the chamber where the two air masses mix to produce fog. The cool air intake duct simulates cool ambient air. The temperature is controlled by a combination of one to three liquid nitrogen cooled copper coil heat exchangers placed in series. Smoke from smoldering fire and water vapor from a humidifier are feed directly into the heated intake duct. The temperature in the heated air intake duct is increased using a heat gun. The flow through the two ducts is directed by fans with adjustable speed in each duct. The contents from both ducts mixes in the optically clear acrylic box where fog formation was observed. Campbell Scientific HMP45C probes were placed at the inlets and

exit of the acrylic chamber for measuring temperature and relative humidity before and after mixing. Vane probe anemometers are placed in the ducts to calculate the volumetric flow rate through the ducts. Main parts of the inlet ducts are marked on a photograph in Figure 3.3.

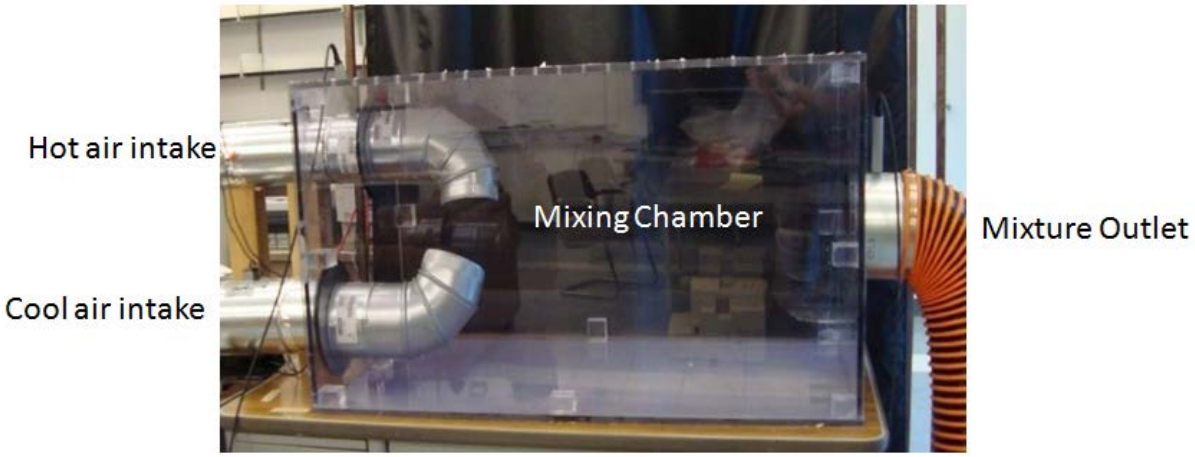

Figure 3.2. Superfog transparent acrylic mixing chamber

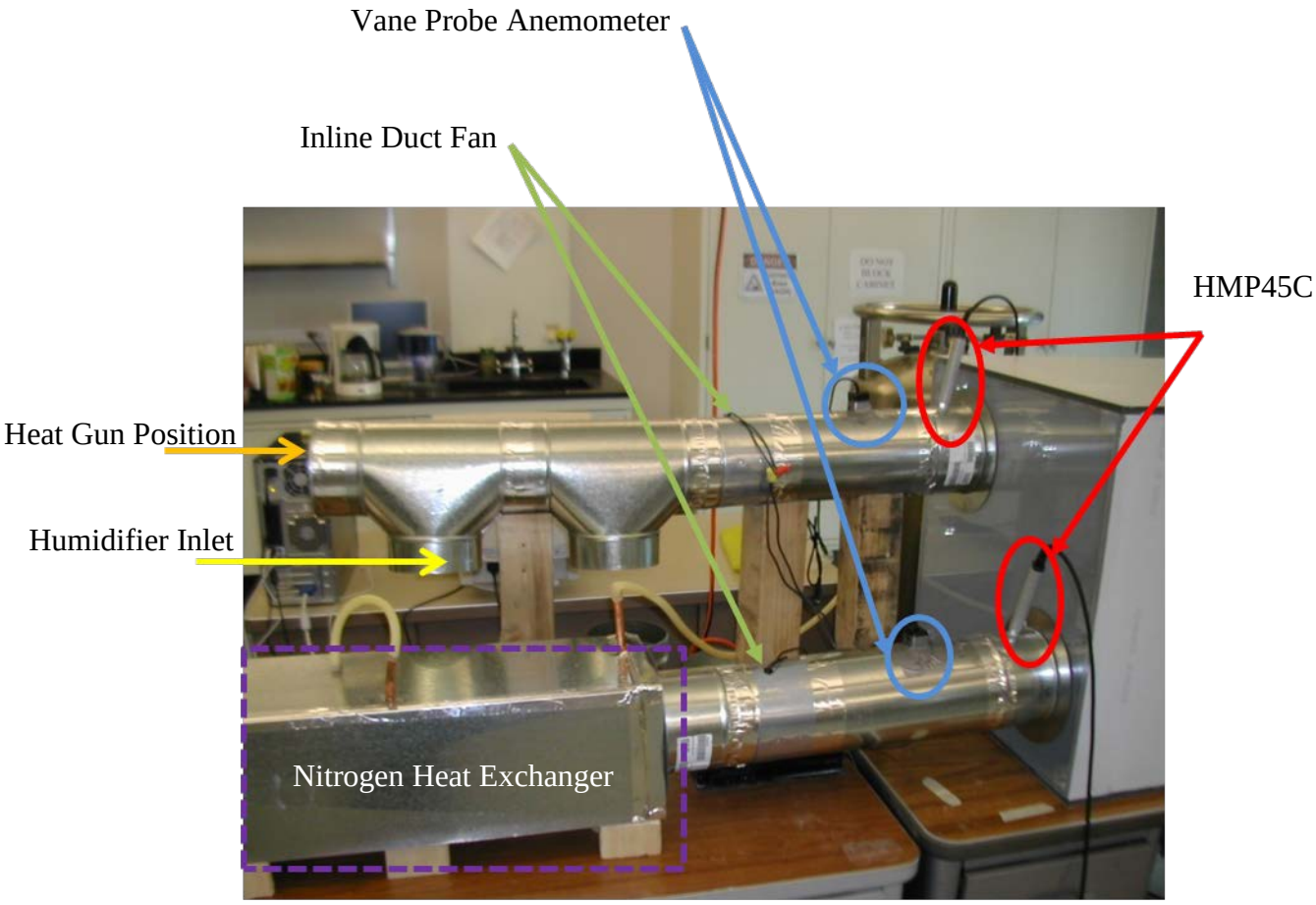

Figure 3.3. Photograph of the inlet ducts to the acrylic mixing chamber. Locations of main parts, including cool air heat exchanger, vapor inlet, CCN inlet, fans, anemometers, temperature and relative humidity sensors (HMP45C), are marked.

3.1.2. Small Fog Chamber Measurements

Initial set of experiments consisted of taking pictures of fog formation events within the chamber using a digital camera under various inlet conditions. Figure 3.4a provides a base visibility and depth of vision prior to the fog formation experiment. An image taken during a fog formation experiment is given in Figure 3.4b. In the experiment photo the background cabinets and labeling on them are no longer visible. The orange chair which is 4 feet away from the chamber can barely be seen where the metal arm rests show up in the experiment photo but the color is undetectable. The top warm air duct's visibility in the experiment photo is greatly diminished although it is only 1.5 feet from the front side of the Superfog box.

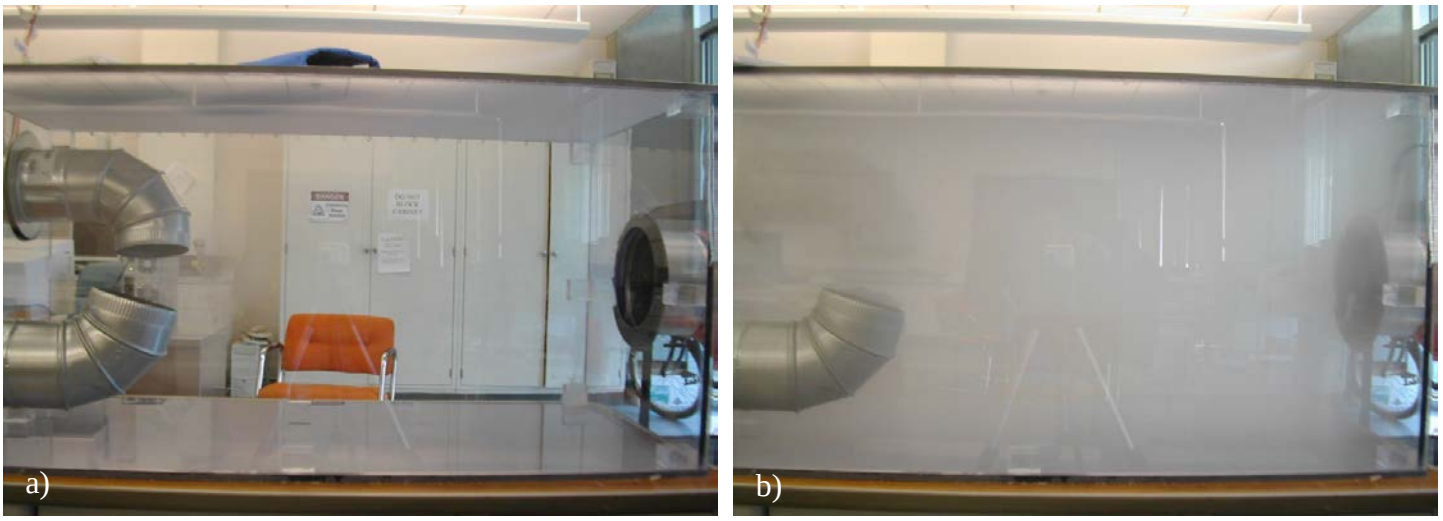

Figure 3.4: (a) The left pane presents the Superfog box mixing chamber volume before warm and cool air masses are mixed. (b) The right pane presents the Superfog chamber during a fog formation experiment causing visibility to dramatically decrease limiting the clarity of background cabinets, the orange chair, and top inlet duct.

This type of simple visualizations (Figure 3.4) provided decent qualitative measure of fog formation based on the decrease of visibility but we needed quantitative results. Based on presented relations between droplet size distribution and number concentrations in Section 2 we were able to develop a method to approximate the visibility distance. However, a particle size distribution within the chamber was needed as an input. We deployed a TSI Phase Doppler Particle Analyzer (PDPA) to measure the droplet size distribution and number concentration of fog formed within the mixing chamber.

Two experiments were conducted and the droplet size distribution and number concentration were measured using the PDPA system. Both experimental conditions are given in Table 3.1. Five repetitions were made for each experimental setting. The temperature and relative humidity of both inlets and the outlet were sampled at 10 Hz and stored in CR5000 Campbell Scientific data logger. Mixed exhaust was ducted to the PDPA system for sampling. The conditions and measurements were averaged for the 5 repetitions of each experiment. The averaged particle size distribution for both experiments is given in Figure 3.5.

Table 3.1: Superfog mixing chamber experimental parameters for PDPA Measurements

Parameter	Experiment 1	Experiment 2
T_1 [^{o}C]	32.2	27
RH_1 [%]	96.1	61.8
w_1 [g kg^{-1}]	31.74	14.62
T_2 [^{o}C]	8.1	11.1
RH_2 [%]	99.1	98.1

w_2 [g kg^{-1}]	6.76	8.08
T_3 [^{o}C]	17.9	14.9
LWC [g m^{-3}]	5.4	1.9
Particles [# ccm^{-1}]	49000	20000
Visibility [m]	1.7	5

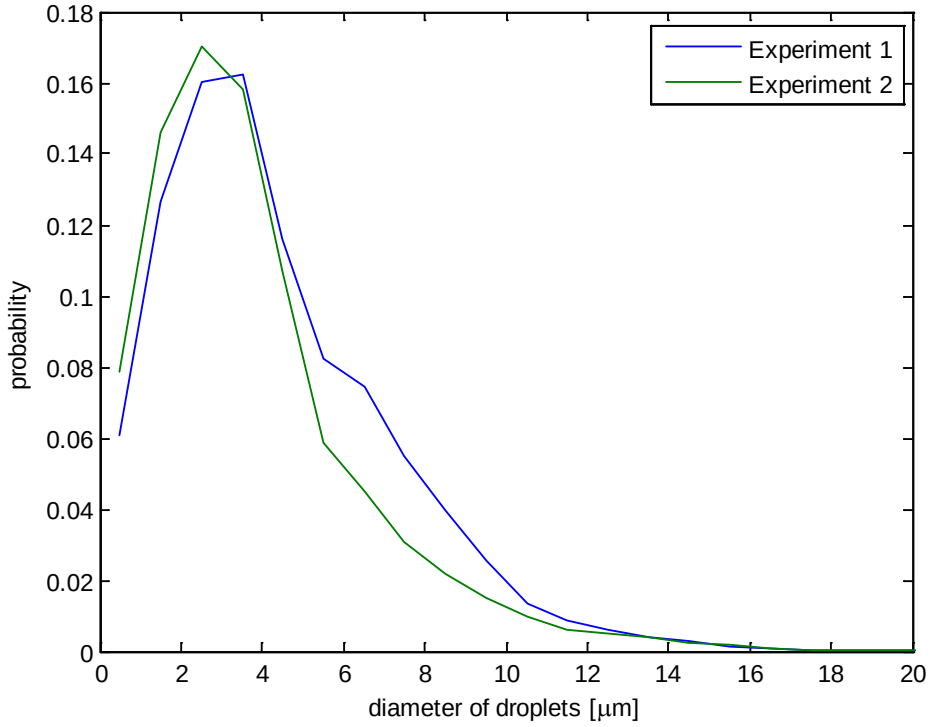

Figure 3.5. Averaged results of fog droplet size distribution from two Superfog box experiments recorded by PDPA system.

We see that the general shape of distribution is very similar for the two experiments. Distributions show discrepancy in the ranges from 5 to 12 micrometer droplets. There was no additional CCN added to the mixture other than existing ambient CCN.

Using the Superfog chamber we were able to generate a fog through thermodynamic mixing and we were able to produce fogs with Superfog visibilities. The Superfog formed here provided certainty in the ability to produce fog and provide us knowledge of the challenges in controls involved so that we could better plan the needed modifications and the experiments for the wind tunnel. PDPA measurements were useful for determining droplet size distribution. The droplets formed were double the expected size of the sensitivity modeling. The sensitivity modeling conducted suggested superfog visibility required small droplets to form in situations where *lwc*

was sparse. Superfog formed in experiment 1 was able to form because the droplet density increased and as expected *lwc* was higher.

3.2 Wind Tunnel

The wind tunnel located at the U.S. Forest Service PSW Research Station in Riverside, CA, was modified for study of the environmental and fuel variables that favor Superfog formation. Pine needle fuel with varying configuration and moisture content was burnt in the wind tunnel, and the relative humidity and temperature of the inflow air are varied. The temperature and humidity are measured at several locations to study the evolution of the fog, and the visibility is determined using a custom designed instrument that measures laser light transmission. This newly designed instrument for this project will be explained in section 3.2.2.5. Through experimentation, we have identified combinations of environmental and fuel variables that replicate Superfog visibilities.

Three different sets of experiments were conducted:

(1) Experiments to determine smoke properties,

(2) Experiments for Superfog Formation,

(3) Experiments to measure boundary layer development.

Smoke measurements focus on characterizing the smoke properties such as temperature, humidity and heat flux. Superfog formation experiments investigate various combinations of fuel bed moisture content, ambient wind, temperature and humidity conditions to form or not to form Superfog. The boundary layer experiments were conducted to validate the new model for smoke plume growth.

3.2.1. Wind Tunnel Description

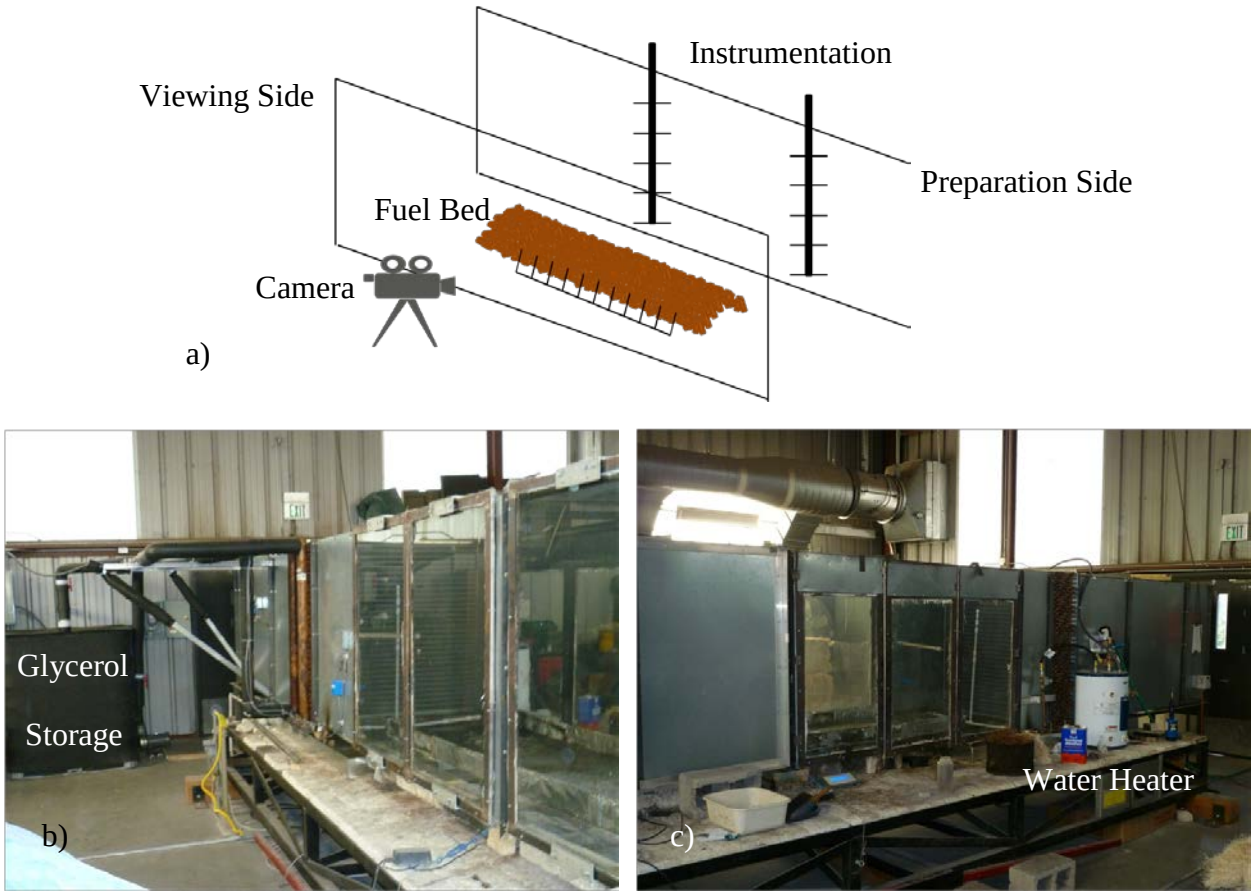

Figure 3.6: (a) Simple schematic of the wind tunnel and instrument locations. (b) The photograph shows the viewing side, plumbing and glycerol storage for wind tunnel's climate control system. (c) The photograph shows the preparation side of the wind tunnel where tank walls are doors that opens for preparation and placement of fuel bed. The preparation side photo also shows the water heater used to generate water vapor to control the ambient relative humidity within the wind tunnel.

Modifications to the wind tunnel specific to this project included the addition of ambient temperature and humidity control. The incoming air temperature is cooled by custom made copper heat exchanger and air conditioning system designed and manufactured by a contractor, Mr. Gary Long from A + AIR Corp. Working fluid through the heat exchanges is Glycerol. Glycerol is cooled by an industrial air conditioning unit outside the burn building. Schematic of the cooling system is given in Figure 3.7. To enable longer experimental duration and lower temperatures, a glycerol storage tank is added. During the preparation stage the glycerol is circulated through the heat exchanger and the storage tank until the temperature of glycerol was below 20 deg F. For the experimental runs, the cool glycerol was recirculated through the heat

exchanger installed in the wind tunnel. Pictures of the main parts of the cooling system are given in Figure 3.9.

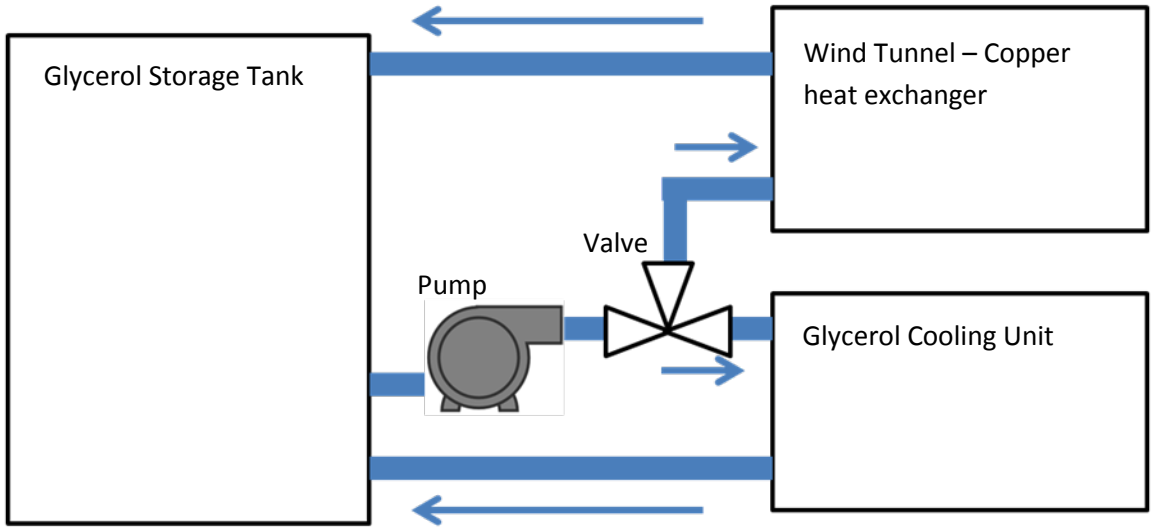

Figure 3.7. Schematic of the wind tunnel temperature control loop. In the cooling stage, in the morning of each experimental day, the valve would be set to allow glycerol to flow between the storage tank and cooling unit. During the experiments the flow would be redirected from the Glycerol storage tank to the wind tunnel heat exchanger.

Figure 3.8. a) Photo of the glycerol cooling unit located outside the burn building, b) the glycerol storage tank located inside the burn building, c) side view of the heat exchanger

The pump speed is controlled by an air temperature sensor directly downstream of the heat exchanger. Pump speeds are modulated to maintain the desired ambient air temperature for the

experiment. Humidification for the wind tunnel is produced using a water heater. The water vapor was injected inside the tunnel via set of nozzles (figure 3.9) after the heat exchanging element. A relative humidity sensor is placed downstream of the nozzles. The release of moisture from nozzles is controlled by a regulator to maintain desired relative humidity.

Figure 3.9. (a) Water vapor is released by nozzles horizontally at the bottom and vertically through the middle directly after the air cooling heat exchanger. (b) Water heater located outside the wind tunnel provides heating and storage of water for wind tunnel humidification.

3.2.2 Instrumentation Description

Numerous instruments were used to quantify the properties of the smoke and fog formed in the wind tunnel. A Campbell Sci. sonic anemometer CSAT3 was used in the early experiments to quantify the temperature and vertical velocity fluctuations for the estimate of the heat flux from the smoldering fuel bed. Fourteen k-type thermocouples were used to create vertical and downwind surface temperature profiles. The Campbell Sci HMP45C temperature and relative humidity sensors used in the test chamber experiments were also used to sample smoke characteristics. To obtain the CCN concentration produced by the smoldering smokes TSI Dust Trak was used for sampling PM1. Infrared (IR) camera was used to measure the temperature of the fuel bed. Temperatures measured from IR camera are presented in table 3.2. Huskeflux heat flux sensor was also used to measure the heat from smoldering fires. A custom visibility senor

was developed to measure visibility through smoke. Some instruments are outlined in the following sections.

3.2.2.1 Sonic Anemometer CSAT3

A Campbell Sci. sonic anemometer CSAT3 was used in the early experiments to quantify the temperature and vertical velocity fluctuations to estimate the heat flux from the smoldering fuel bed. CSAT3 has a 10 cm vertical measurement path. 3D velocity and temperature were sampled at 10 Hz and stored by CR5000 data logger. The CSAT3 uses a FW05 fine wire thermocouple (12.7 μm diameter). Offset error in vertical direction is within 4.0 cm s^{-1}. Figure 3.10 presents photographs of the CSAT3 deployed for measurements (a) and close up (b).

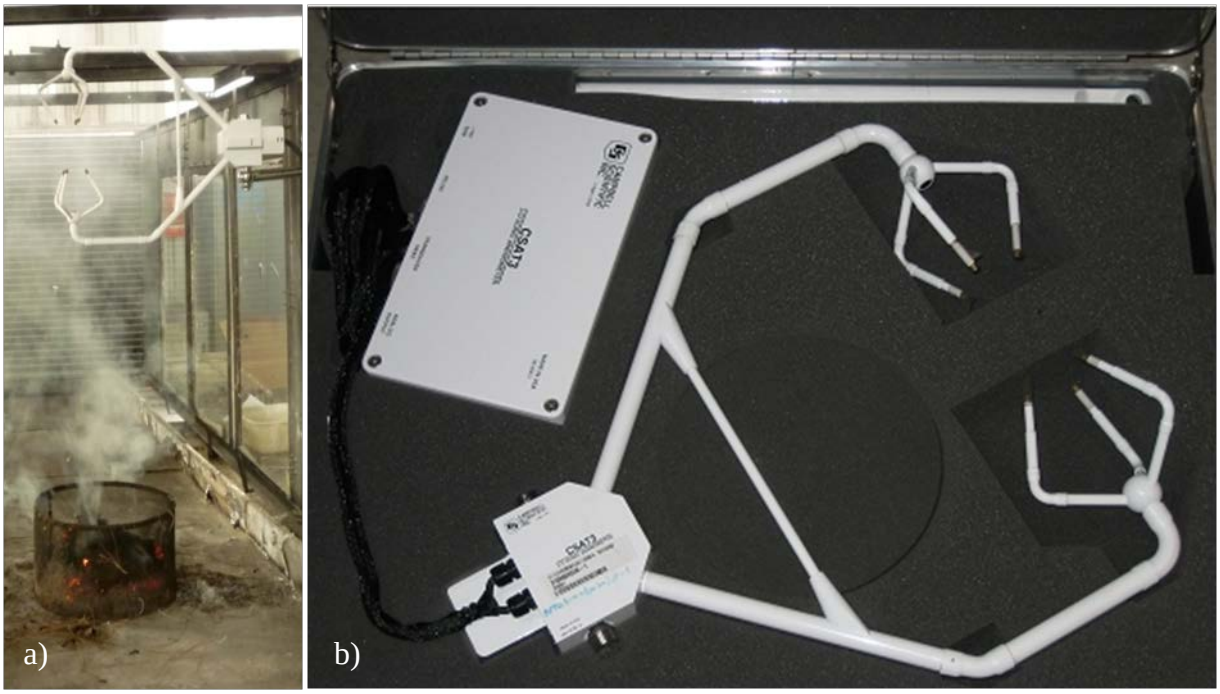

Figure 3.10. Campbell Scientific sonic anemometer (CSAT3). The photo on the left shows the implementation of the CSAT3 device. The photo on the right shows a larger image of the CSAT3 and signal converter box.

3.2.2.2 Heat Flux sensor

Huskeflux RC01 radiation and convection heat flux sensor was used to measure the heat from smoldering fires. The RC01 uses the combination of two heat flux sensors. The first is covered by gold reflector, thus sensitive only to convective heat transfer. The second is the black panel which is sensitive to both convective and irradiative transfer. The RC01 has external thermocouple to measure surrounding air temperature. This device allowed us to measure convective and radiation heat transfer from the smoldering fuel bed.

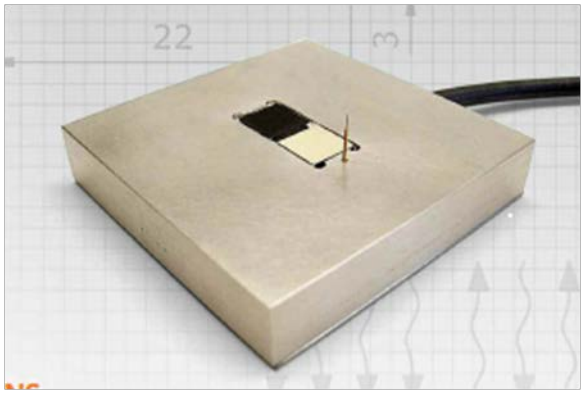

Figure 3.11. Hukeflux RC01 heat flux sensor (www.huksefluxusa.com)

3.2.2.3 Temperature and Relative humidity sensors

Fourteen k-type thermocouples were used to create vertical and downwind surface temperature profiles in the Boundary Layer experiments. Five thermocouples were used in smoke measurements (Figure 3.12). The Campbell Sci HMP45C temperature and relative humidity sensors used in the test chamber experiments were also used here to sample smoke temperature and relative humidity.

Figure 3.12. The HMP45C temperature and relative humidity deployed with k-type thermocouples to measure smoldering smoke temperature and relative humidity

Figure 3.13. Thermocouples are placed along the down wind direction and vertically above the fuel bed to measure temperature profiles of smoldering smoke. a) Upwind view of wind tunnel where undergraduate students prepare pine needle fuel bed and thermocouples. b) View of the thermocouples from preparation side of the wind tunnel.

3.2.2.4 Particulate Sampling

TSI Dust Trak Aerosol Monitor (Figure 3.14) measures particle concentrations of PM10, PM2.5, and PM 1.0. Dust Trak uses laser photometer with 90^{o} light scattering. It can measure concentrations from 0.001 to 100 mg m^{-3}. To measure CCN concentration produced by the smoldering smokes TSI Dust Trak sampled PM1 particle concentrations.

Figure 3.14. TSI Dust Trak (www.tsi.com)

3.2.2.5 Visibility sensor

We custom designed a visibility sensor to quantify the visibility through the resulting fog in each experiment.

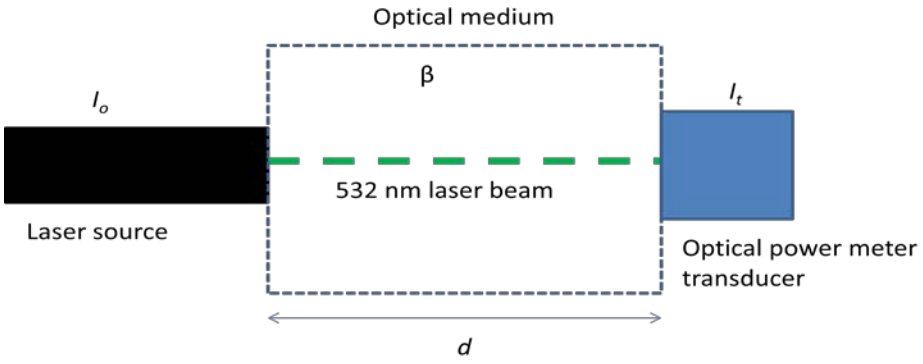

Figure 3.15. Schematic of custom visibility meter

The new visibility meter deploys the Beer-Lambert law to calculate the extinction coefficient, β, of the medium through which the laser passes as

$$\ln\left(\frac{I_t}{I_o}\right) = -\beta d \tag{3.1}$$

where I_t is the power measured at the optical transducer in the smoke and fog, I_o is the power measured in clean air, d is the distance between the laser source and optical transducer, and β is the extinction coefficient of the fog. In our setup the laser head is 10 cm from power meter transducer.

The visibility and the extinction coefficient are related as

$$vis = -\frac{\ln \mu}{\beta} \tag{3.2}$$

where μ is the limit of contrast usually taken to be a value of 0.02 and *vis* is the visibility.

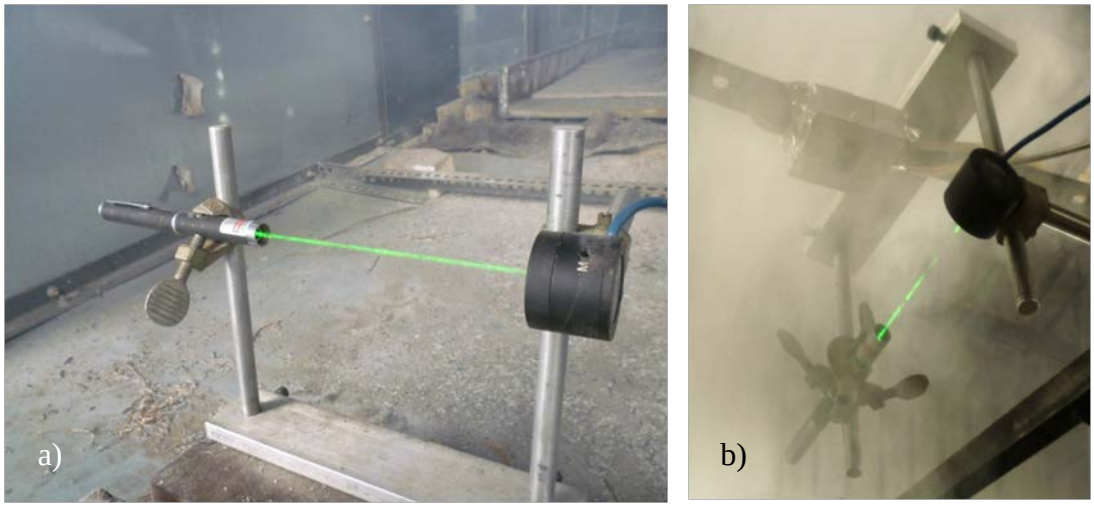

Figure 3.16. Photo of implemented visibility meter. The photograph on the left shows visibility meter at the exhaust end of the wind tunnel. The photograph on the right shows visibility meter located above a smoldering fuel source without crosswind.

3.2.2.6. Fuel moisture Content

To create different fuel moisture contents in the experiments the pine needles were soaked in water prior to the experiment (figure 3.17a).

Figure 3.17. a) Pine needles are soaked for short period of time between 1 and 5 minutes to achieve different fuel moisture content values. b) In the first configuration pine needles are placed into the wire mesh fuel bed configuration. Wire mesh fuel container 0.3 meter in diameter and .3 meter height. c) In the second pine needle configuration pine needles are spread over the entire space of the burn platform within the wind tunnel.

A sample of pine needles is taken from each experiment and is stored in a bottle for later fuel moisture content analysis (figure 3.18a). The mass of each bottle is known before use and is subtracted from the total mass of bottle with fuel. Fuel moisture content is measured by first weighing the mass of the bottle with the fuel sample. Next, the bottle is placed into an oven with

lid open (figure 3.18b). After 24 hours, the bottle is weighed again. The difference in mass is the water evaporated from the pine needles. Fuel moisture content, *fmc*, is measured using the formula

$$fmc = \frac{m_w - m_d}{m_w} \bullet 100 \tag{3.3}$$

where m_w is the mass of wet fuel and m_d is the mass of dried fuel.

Figure 3.18. a) Fuel samples are taken of the treated fuel beds used in experiments. b) Fuel sample bottle are placed in oven and heated for 24 hours to evaporate water.

3.3. Experimental Set 1: Smoke Measurements

The first set of experiments conducted was used to determine the smoke properties: temperature, humidity, CCN concentration and heat flux. Pine needle fuel source was placed into the wire mesh cylinder (figure 3.19b). Fuel bed masses ranged from 200-500 grams. These initial experiments were conducted without cross wind. After ignition, fuel bed goes through flaming, flaming/smoldering, and full smoldering phases (figure 3.19). Instrumentation is deployed after full smoldering phase begins to prevent damage to the instrumentation due to the high heat during the flaming phases (figure 3.19a). All measurements were recorded by the CR5000 data logger except the Dust Trak since it has the internal memory storage capabilities.

Figure 3.19. After the fuel bed is prepared it is ignited. It goes through a) the flaming phase, b) the combination of flaming and smoldering, and c) smoldering phase. To prevent damage by flame, instruments are placed into the smoke when fuel bed has reached full smoldering phase.

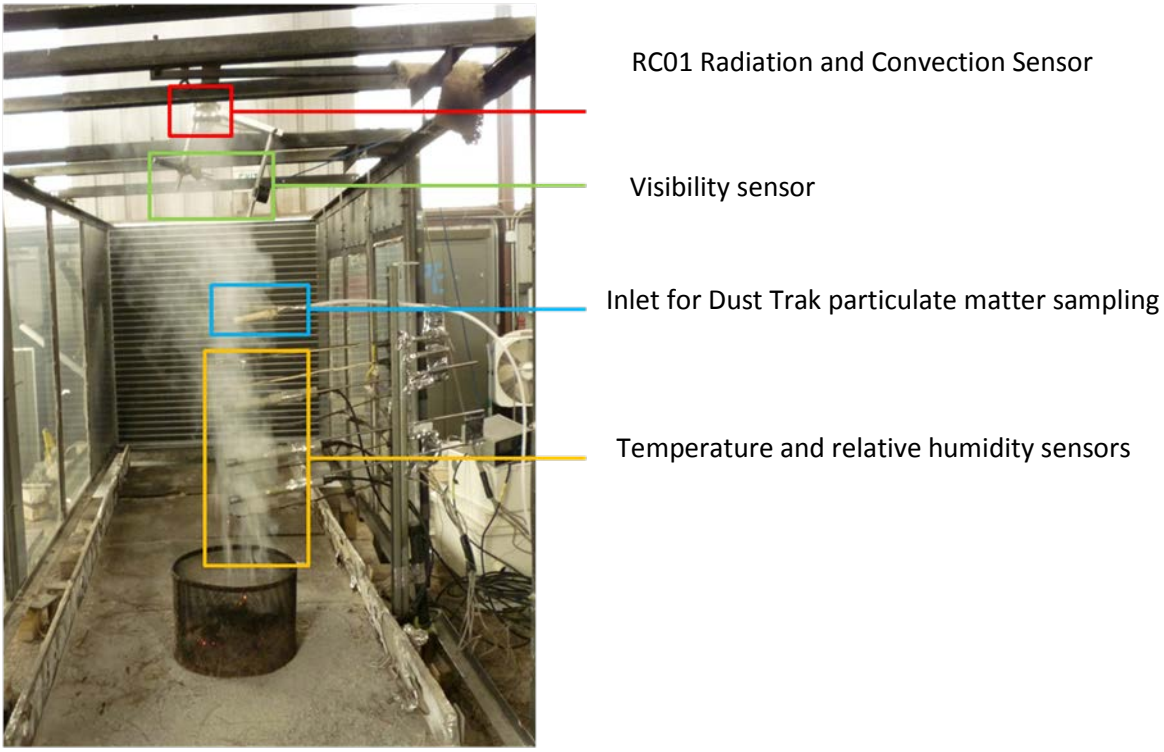

Figure 3.20. Placement of radiation heat flux, visibility, particulate matter, temperature and humidity sensors for smoke measurements.

The first parameter measured from smoke was the heat flux. The CSAT3 was located 1 meter above the fuel bed. Figure 3.21 shows the results for 9 experiments. The time zero is the start of measurements during the smoldering phase. Measurement phase is cut off at time where fuel bed is extinguished and no longer producing smoke. We can see from measurement results that initially smoldering convective heat flux can be as high as 3.5 kW m^{-2}. As time continues smoldering produces heat flux of 1 kW m^{-2} before ceasing to combust.

The heat flux was also measured by the RC01 sensor. As before, time zero is the time of implementation of instrument 1.5m above smoldering fuel bed. Five experiments are presented in figure 3.22 showing the measured convective and irradiative heat transfer. We see that both convective and irradiative fluxes are generally below 0.5 kW m^{-2}. Spikes early in the plot can be attributed to flames that may from time to time appear as small pockets of the fuel bed re-ignite.

The particulate concentration is measured for 5 experiments. Initial time zero begins at time of instrument implementation. There are great fluctuations of concentration of PM1 between 10 and 180 mg m^{-3} which is the saturation value for our instrument.

Visibility through the fog created from these experiments was measured using our custom visibility meter. Examples of power meter recordings for two of the experiments are given in figure 3.23 and 3.24. If we take a look at figure 3.23 for experiments 30, we see that the initial

power value is around 60mV and it approaches 40mV in the presence of smoke. Using equation 3.1 we can see that the extinction coefficient of the smoke formed in experiment 24 to be 4.05 m^{-1}. We can determine the visibility to be 0.96 m by use of equation 3.2.

Measurements of fuel bed temperature, smoke temperature, smoke humidity, visibility and fuel moisture content are summarized for 10 experiments in Table 3.1.

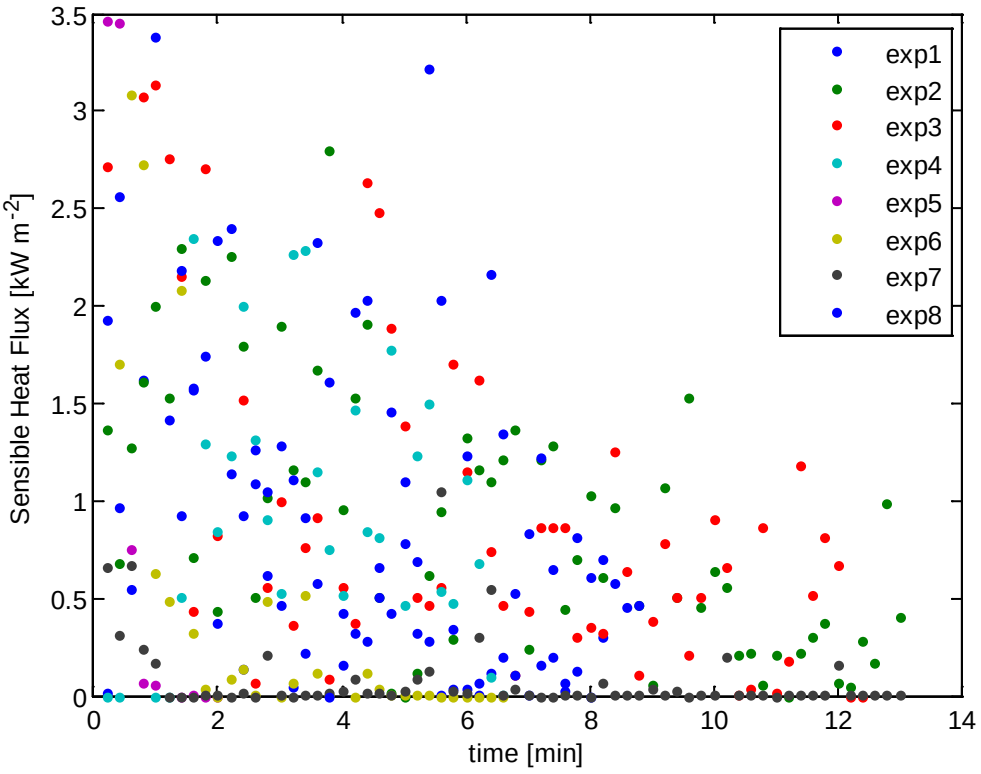

Figure 3.21. Sensible heat flux results of smoke above fuel bed using measurements from CSAT3 anemometer.

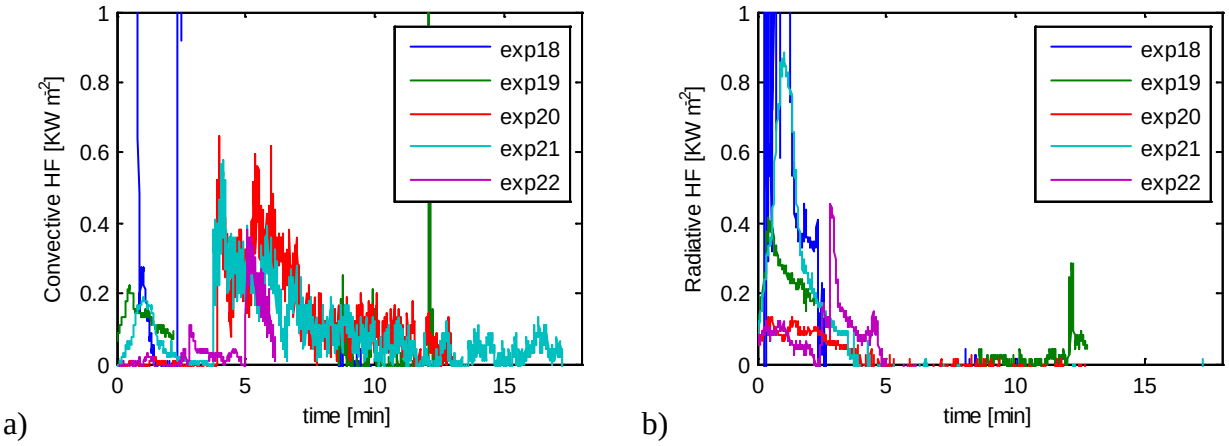

Figure 3.22. a) Convective and b) irradiative heat flux measurement 1.5m above a smoldering fuel bed using RC01 sensor.

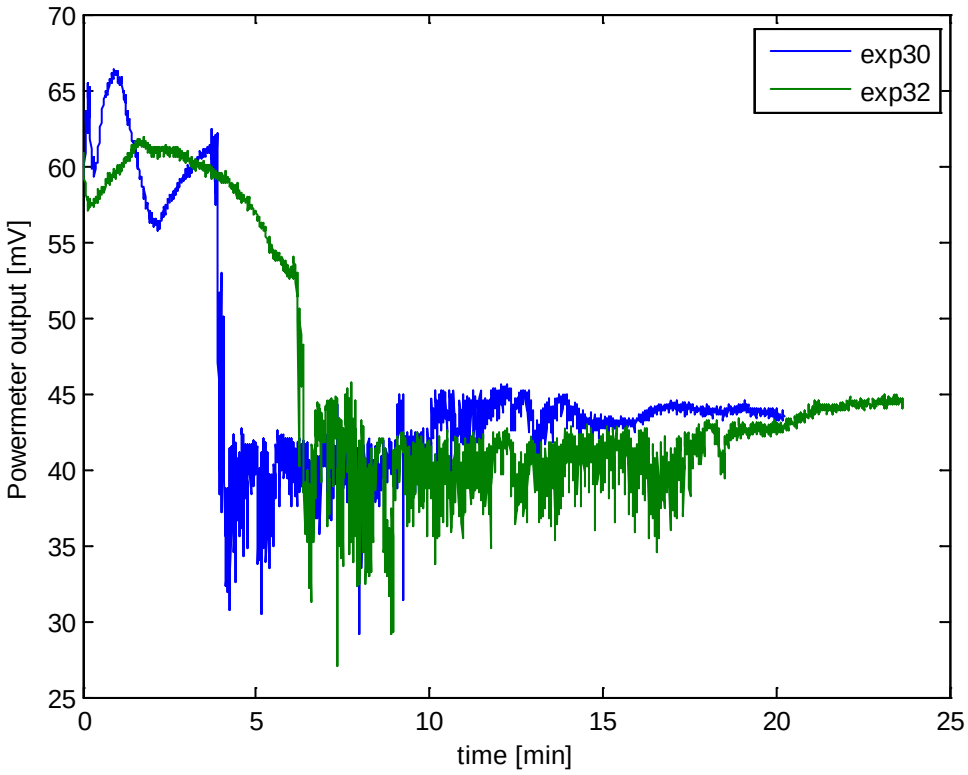

Figure 3.23. Voltage signal from optical power meter for experiments 30 and 32.

Table 3.2. Summary of smoke measurements

Smoke Experiment Number	Fuel Moisture Content [%]	Visibility [m]	Fuel Bed Temperature [^{o}C]	Smoke Temperature [^{o}C]	Relative Humidity [%]
23	28	1.7	200	40-80	10-50
24	29	3.2	300	30-100	10-50
25	41	0.9	150	40-90	10-50
26	20	0.9	50	50-90	4-45
27	25	0.4	200	40-80	4-45
28	7	0.4	300	40-60	4-45
29	39	1.2	100	28-32	39-42
30	24	2.5	200	45-80	5-20
31	12	1.0	300	50	2
32	30	0.8	100	60	5-12
33	28	1.7	150	40-50	5-12

The measurements conducted in the smoke measurement section provided us with smoke parameters to use inputs into the 2D boundary layer dispersion model which was introduced in Section 2.

3.4 Experiment Set 2: Controlled Superfog Formation

The goal of Superfog Formation Experiments is to build upon smoke measurements by introducing and controlling cross wind, ambient temperature, humidity and fuel moisture content in order to form Superfog. First we recreated conditions from known Superfog events:

(1) I-4 in Polk County, FL on January 9 2008,

(2) I-75 near Gainesville, FL on January 31, 2012,

(3) Dismal Swamp, VA in 2011.

We designed experiments to investigate temperature and humidity conditions in vicinity of observed temperature and humidity from these historical events. Table 3.4 summarizes the test conditions used in the experiments. Figure 3.24 is a simple schematic of the setup used for these experiments.

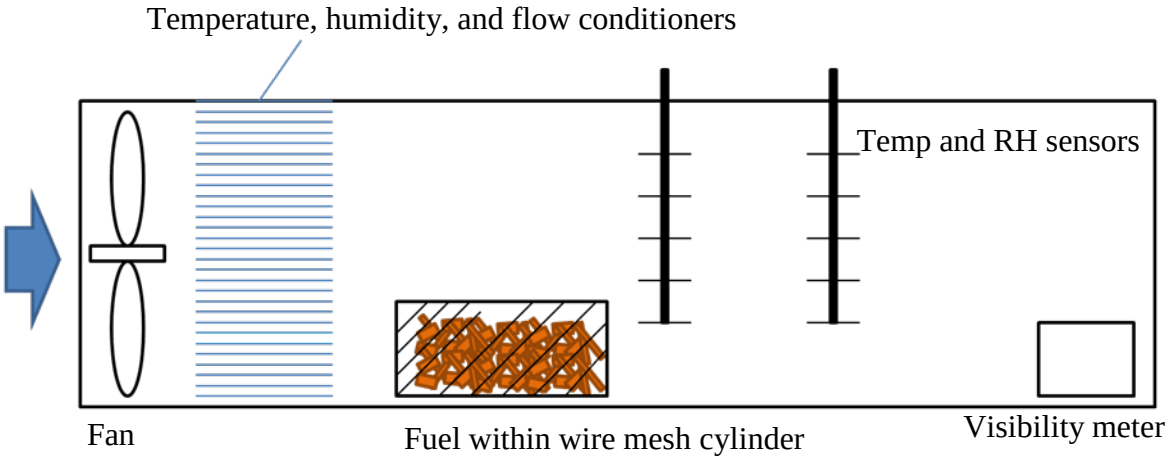

Figure 3.24. Simple schematic of Superfog Formation Experiments setup.

From our experience, smoke forms more readily when the fuel bed is in a piled up orientation instead of being spread throughout the wind tunnel floor. In the tightly packed configuration less oxygen is allowed to react, thus decreasing combustion rate. This produces a lower intensity and longer lasting smoldering. For this reason we chose to use the same wire mesh used in the smoke measurements for the fuel bed shape. In the incidents occurring in Florida, which resulted in the major car pileup in the early morning hours prior to sunrise, wind speeds were recorded to be near zero (wunderground.com). Low wind velocities were also recorded during the I-10 event in New Orleans, Louisiana in 2011. The smoke had traveled from burn areas to freeways at some small velocity. Consequently, for the wind tunnel experiments we used very low wind speeds. Speed controller for wind tunnel's fan was set to 26.7 Hz producing wind velocity of approximately 0.5 m s^{-1}. This wind velocity was used for all the experiments. This

velocity was chosen as the lowest velocity that our wind tunnel is capable of maintaining without major fluctuations. The low wind velocity allows sufficient time for vapor to condense in the cool surrounding air allowing Superfog to form within the length of our wind tunnel. If the Superfog forms under this velocity it would definitely form and for lower wind velocities. Temperature and humidity sensors were located downwind of the fuel bed. The custom visibility meter was placed at the exit of the wind tunnel. A photo of an experiment from the viewing side of the wind tunnel is presented in Figure 3.25.

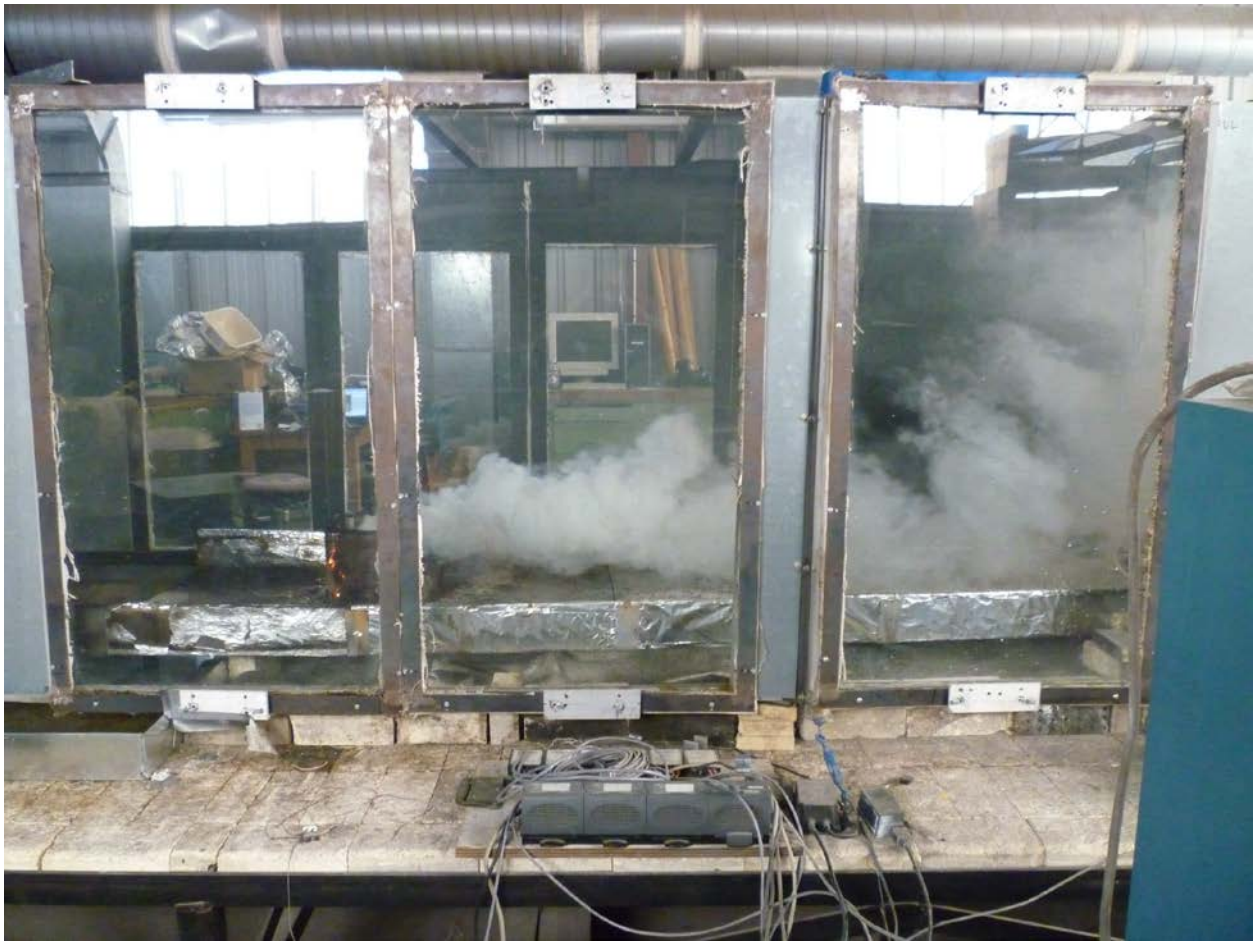

Figure 3.25. Viewing side of wind tunnel during a Superfog formation experiment.

3.4.1. Experimental Procedure

On experiment days, glycerol would be cooled and water heated for humidity production in the morning hours. The climate control system in the wind tunnel can produce temperatures as low as 20 degrees Fahrenheit less than the local ambient temperatures. This gave us the lower limit of temperature for experiments on any given day. Desired ambient temperature and humidity values within the tunnel are chosen and values set into the wind tunnel controls. Pine needles are

treated by water bath to increase their fuel moisture content (see Section 3.2.2.6). Treated pine needles are weighed to 400g and placed into the wire mesh container. Excelsior, 50g, is added to the fuel bed to assist in ignition. After the fuel bed is set in place, the fan and climate control system is activated. Fan speed is set to maintain 0.5 m/s wind speed. The glycerol flow valve is adjusted to allow flow between the storage tank and the wind tunnel heat exchanger only. Pump speed is automatically modulated by the speed controller to maintain desired set temperature for that experiment. The humidity control loop is turned on and the desired humidity is set. Nozzles within the tunnel release water vapor as needed to adjust the humidity. Measurements of air and vapor temperature used to provide feedback for the tunnel climate controls were independent from our temperature measurements of smoke. After the desired conditions inside the wind tunnel are met, the fuel bed is ignited. Data logger recorded readings from the instruments throughout the day. Time of ignition, start of smoldering phase, and end of experiment was recorded for later analysis. Experiments were also recorded by a video camera. The experiment checklist is given below. Duration of major experimental steps is summarized in Table 3.3. For more detailed instructions on use of wind tunnel please see Appendix A.

3.4.2. Experiment Checklist

1. Cool glycerol
    a. Change valve position to storage tank and cooling unit flow loop
    b. Cool glycerol to 20^{o}F
2. Heat water for humidification
3. Determine desired wind tunnel temperature and humidity
4. Prepare fuel bed
    a. Treat fuel to add moisture
    b. Prepare 400g fuel bed in wire mesh
    c. Save fuel sample for *fmc* analysis
5. Cool wind tunnel
    a. Adjust valve to transfer glycerol flow between storage tank and wind tunnel heat exchanger
    b. Set target temperature in wind tunnel controls for temperature
6. Humidify wind tunnel
    a. Set target humidity
7. Allow time for wind tunnel to achieve target temperature and humidity
8. Place fuel bed into the wind tunnel and ignite
9. Record start time, smolder time, and experiment end times

Table 3.3. Duration of major experimental parts

Procedure	Duration
Glycerol cooling and water heating stage	2-4 hours
Water immersion treatment for pine needle fuel bed	2-10 min
Steady target temperature within wind tunnel	5-20 min
Ignition to smoldering phase	2-10 min
Smoldering phase	10-40 min

A summary of experimental temperature ranges is given in Table 3.4. Experiment numbers are placed in the table corresponding to the wind tunnel temperature and humidity. Highlighted regions indicate climate conditions corresponding to known weather conditions associated with Superfog formation. The fuel moisture content values for fuel beds are summarized in Table 3.5. The measurement results for smoke temperature, humidity, and visibility are provided in tables 3.6, 3.7 and 3.8 respectively. Smoke temperature was 10-15 degrees Fahrenheit higher than ambient conditions throughout the experiments. In photographs taken from the experiments (Figure 3.26) a dramatic difference in the fog thickness is apparent when fuel moisture content is increased while temperature and humidity are kept constant.

Table 3.4. Superfog Formation Experiment Summary

Temp [F]	30	35	40	45	50	55	60
RH[%]							
60							
65			E22	E26			
70				E24		E37	E28d
75			E23/E26	E10d/E24	E25	E30	E15
80			E11	E25	E29	E14	
85			E12		E13		
90			E16	E17			
95	E20/E21	E19	E18	E27	E27		

Note: Experiments are named as ‘E’ followed by the experiment number. Highlighted combinations of temperature and humidity indicate conditions from the actual Superfog occurrences. Blue highlighted cells represent conditions during the I-4 disaster in 2008. Orange cells represent conditions during the Dismal Swamp fires. Red highlighted areas represent conditions during the Gainesville incident in 2012.

Table 3.5. Summary of Superfog Formation Experiment fuel bed *fmc* values [%]

Temp [F]	30	35	40	45	50	55	60
RH[%]							
60							
65			40.49	43.25			
70				40.45			9.73
75			45.51/43.25	9.73/40.54	38.18	44.36	44.98
80			34.69	38.18	40.43	48.1	
85			34.56		45.09		
90			39.01	37.36			
95	38.82/12.12		40.54	40.67	40.67		

Table 3.6. Summary of averaged smoke temperatures [^{o}F]

Temp [F]	30	35	40	45	50	55	60
RH[%]							
60							
65			53.6	59			
70				60.8			69.8
75			50/59	68/60.8	60.8		75.2
80			62	60.8		67.1	
85			57.2		60.8		
90			46.4	53.6			
95	41/41.46	41	50	60.8	60.8		

Table 3.7. Summary of averaged smoke humidity measurements [%]

Temp [F]	30	35	40	45	50	55	60
RH[%]							
60							
65			70	41			
70				40			23.5
75			65/41	40/40	40		40
80			60	40		50	
85			70		60		
90			107	80			
95	100	100	100	44	44		

Table 3.8. Experimental visibility results [m]

Temp [F]	30	35	40	45	50	55	60
RH[%]							
60							
65			0.29	0.29			
70				0.27			0.84
75			.29/.29	3.44/.27	1.27		0.38
80			3.44	1.27			
85			1.28		1.24		
90			0.62	0.26			
95	1.93/.37	0.29	0.59	0.67	0.67		

Figure 3.26. Left photo shows light smoke forming from the pine needle fuel bed under ambient temperature of 41^{o}F, 76% relative humidity, and 7 % fuel moisture content. In the right photo, Superfog forms from the pine needle fuel bed under ambient temperature of 43^{o}F, 88% relative humidity, and 40% fuel moisture content.

3.5. Experiment Set 3: Boundary Layer Growth

The third set of experiments conducted in the wind tunnel was used for comparison of or the new numerical 2D boundary layer model introduced in Section 2. In these experiments we focus on the temperature profiles measured by the thermocouples and video footages of smoke. Figure 3.27 shows a simple schematic of our setup in the wind tunnel for the boundary layer experiments. The fuel beds in these experiments were spread out over the floor of the wind tunnel. Table 3.9 notes the horizontal and vertical positioning of the thermocouples. Distances are given in centimeters from the leading edge of the fuel bed for downwind position and from the bottom of the fuel for vertical position. The average fuel bed thickness was 10 to 13 cm (just below the first thermocouple). A photograph of deployed thermocouples can be seen in Figure 3.28.

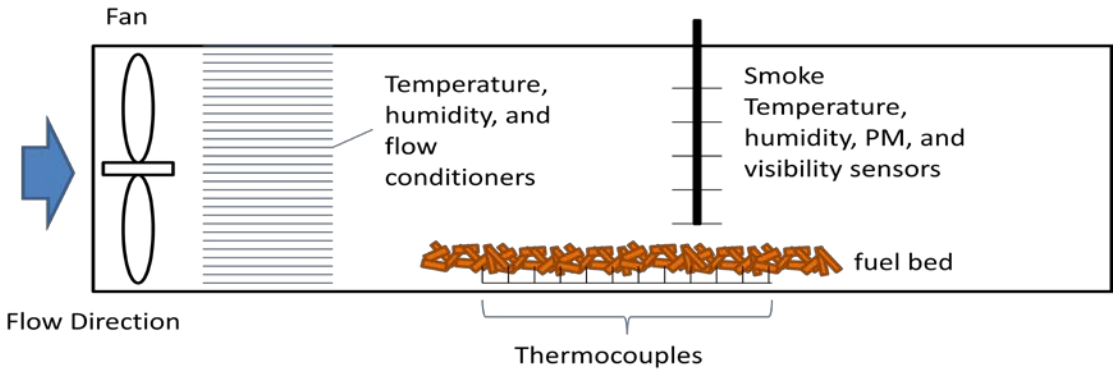

Figure 3.27. Schematic of wind tunnel arrangement for boundary layer experiments.

Table 3.9. Location of thermocouples

Thermocouple Number	Downwind Position [cm]	Vertical Position [cm]
1	75	13
2	97	13
3	119	13
4	139	13
5	163	13
6	181	13
7	202	13
8	218	13
9	239	13
10	260	13
11	181	33
12	181	52
13	181	68
14	181	89

Figure 3.28. Photograph taken during a boundary layer experiment from the preparation side of wind tunnel shows the smoldering fuel bed and thermocouple locations circled in red.

Similar procedure was used for boundary layer experiments as for the Superfog formation experiments. The main difference between the two sets of experiments is the fuel bed shape. While in the Superfog formation experiments we used smaller, circular, fuel bed, for the boundary layer growth investigation we used rectangular fuel bed spread along the wind tunnel. This was the best way to match the model formulation and realistic field conditions. The downwind temperature profiles for the 8 experiments averaged over the smoldering phase are presented in Figure 3.29. Since results from Superfog formation experiments (Section 3.4) show that the fuel moisture content is a major parameter in determining smoke thickness we varied the fuel moisture content while keeping other parameters constant for boundary layer growth experiments. Experimental fuel moisture is given in Table 3.10. Only Experiment 8 was conducted using dry untreated pine needles thus producing higher temperatures. In our measurements we had seen no significant increase in temperature in the downwind direction of the fuel bed. Surface temperature did not shown significant increase because of the short length of the fuel bed. Over larger distances smoldering heat flux could contribute increases in temperature at the surface level. Figure 3.30 provides the vertical profile of temperatures measured 181 cm downwind of the leading edge of the fuel bed. We see a formation of a stable boundary layer in the wind tunnel. Analysis suggests temperature gradients ranging from 24 to 30 $^{o}C\ m^{-1}$. These vertical temperature gradients taken from measurements were used in the boundary layer model.

Table 3.10. Fuel moisture content for boundary layer experiments. Ambient conditions are kept at 15^{o}C and 80% humidity

Experiment	fmc [%]	T [^{o}C]	RH [%]
1	43.25	12.80	45
2	41.58	13.54	34
3	40.43	11.84	45
4	35.97	13.42	52
5	43.25	12.47	30
6	39.01	15.26	52
7	36.79	12.79	52
8	9.02	26.6	35

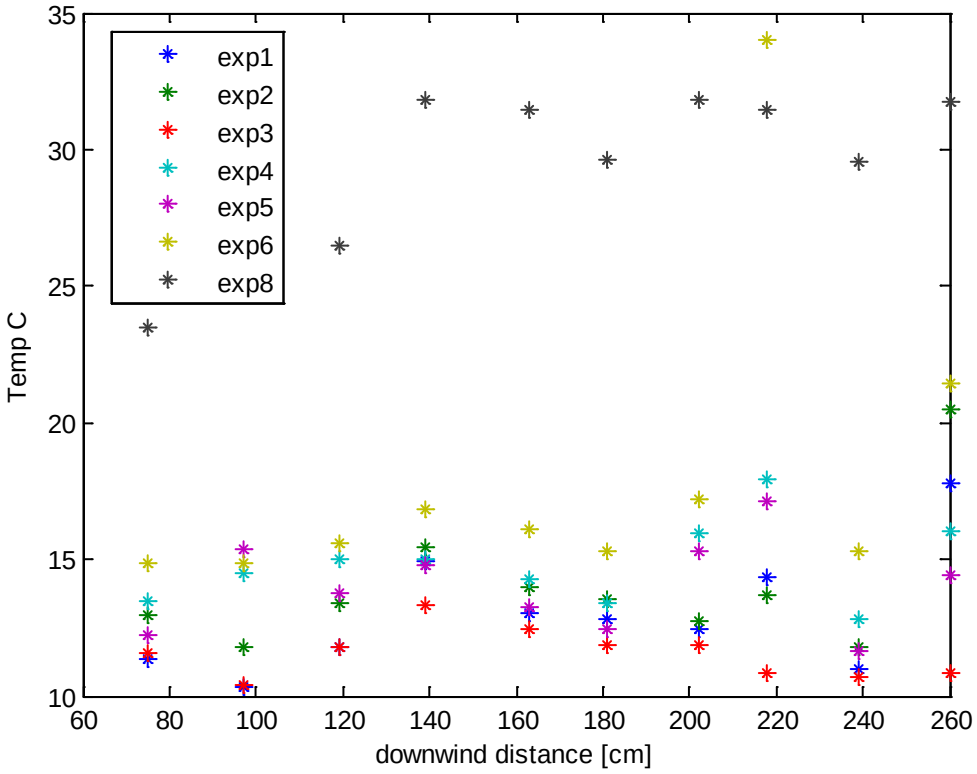

Figure 3.29. Averaged smoldering phase downwind temperature profiles for boundary layer experiments taken at a height of 13cm.

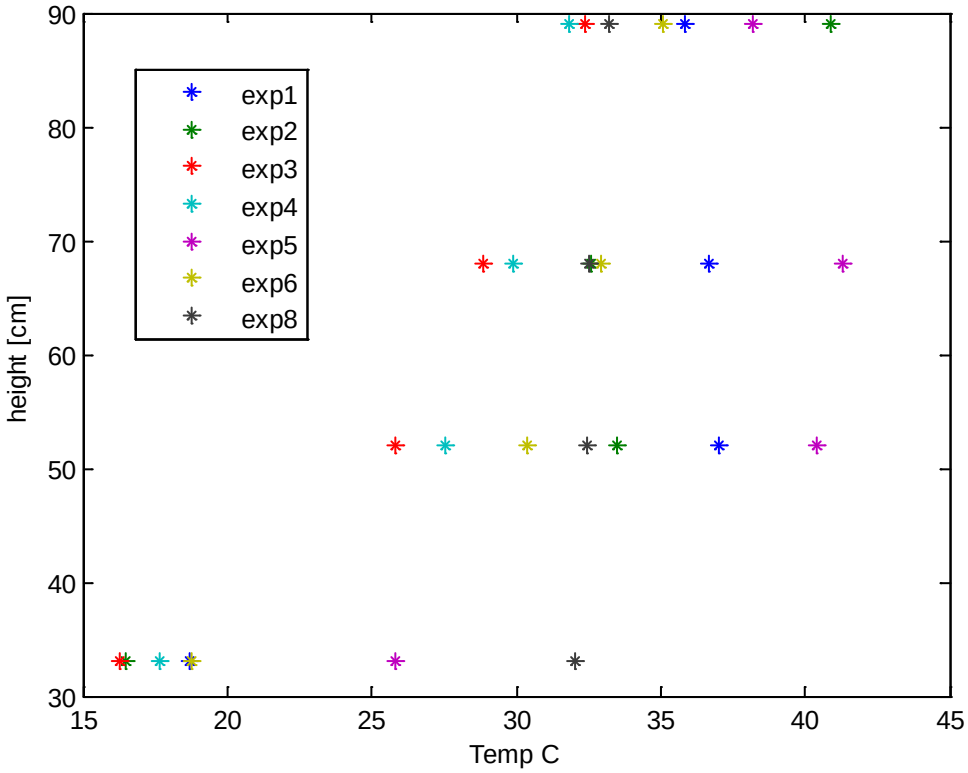

Figure 3.30. Averaged smoldering phase vertical temperature profiles for boundary layer experiments taken at a distance of 181 cm.

It is very difficult to replicate Superfog forming conditions in the wind tunnel with the spread fuel bed configuration used in the boundary layer growth experiment because the availability of oxygen causes most of combustion to occur in the flaming phase leaving little for the smoldering phase, as opposed to the fuel bed inside a cylindrical wire mesh. For this reason, to compare the model results with the experiments we focused on the fog conditions that correspond to the liquid water content of 0.1 g kg^{-1}. This liquid water content corresponds to a visible formation of smoke however not as visually impeding as Superfog that must have at least 2.0 g kg^{-1} of liquid water content. However, this value was good enough to validate the model. Table 3.11 summarizes the experimental parameters that were used as model inputs for validation.

Table 3.11. Experimental settings for model validation

Model Input	Value
Vapor flux	1.6×10^{-3} g m^{-2} s^{-1}
Heat flux	1.0 W m^{-2}
Friction velocity	0.1 m s^{-1}
Monin-Obukhov Length	100 m
Roughness height	0.01 m
Surface Temperature	11.84°C (Experiment 4) 12.79 °C (Experiment 7)
Vertical Temperature Gradient	24.20 °C m^{-1}(Experiment 4) 26.05°C m^{-1}(Experiment 4)
Ambient Relative Humidity	45% (Experiment 4) 52 % (Experiment 7)

We see that the smokes produced in the experiments are within the model prediction heights. Since the model is able to reproduce the experimental boundary layer height we deployed it to predict past field occurrences of Superfog.

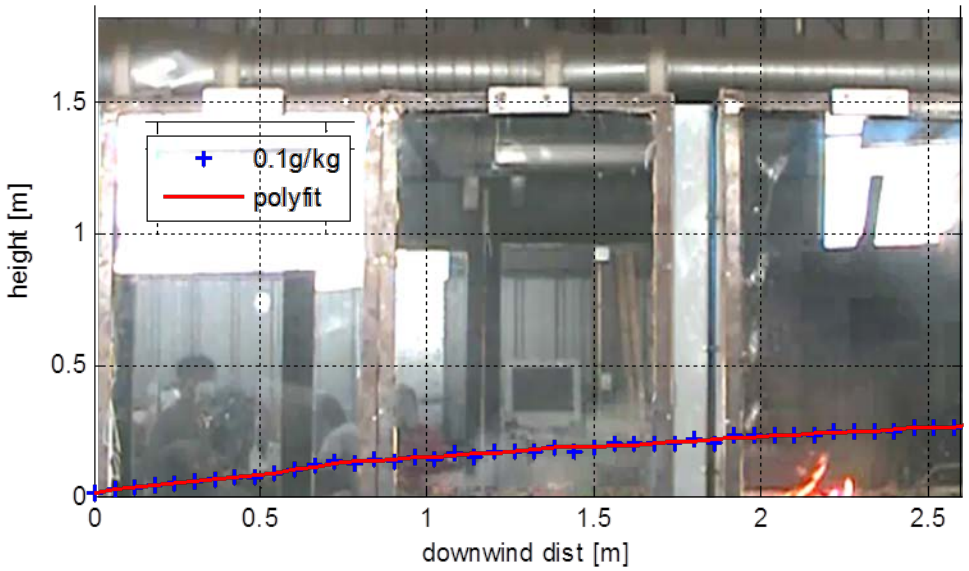

Figure 3.31. Boundary layer experiment 4 photograph from video footage overlapped with model comparison. Model predictions for fog heights with liquid water content 0.1g kg^{-1} are presented in blue. A polynomial fit of the model predictions is provided in red.

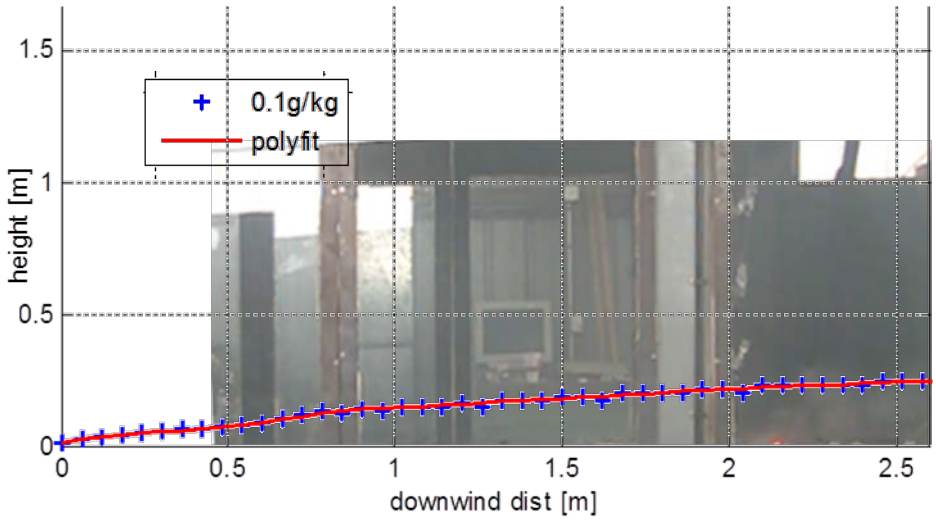

Figure 3.32. Boundary layer growth experiment 7 photograph from video footage overlapped with model comparison. Model predictions for fog heights with liquid water content 0.1g kg^{-1} are presented in blue. A polynomial fit of the model predictions is provided in red.

4. Boundary Layer Model Predictions for Field Incidents

After obtaining key inputs from smoke measurements and validating the boundary layer growth model, the model was deployed to predict the occurrence of Superfog for the I-4 disaster and the Gainesville incidents. A summary of the model input values used for the boundary layer model is presented in Table 4.1. The simulation results are presented in Figures 3.33 and 3.34 for I-4 and Gainesville, respectively. The blue curve represents a polynomial fit of the model data. The red curves are fit of of $x^{1/2}$ dependence with distance x. Based on a criterion of LWC greater than 2.0 g kg^{-1}, we see that in both cases Superfog forms up to a meter high within 30m of fuel bed. For the longer fuel bed Superfog will continue to grow. We see that the growth of Superfog follows $x^{1/2}$ dependence, and the Superfog depth can be expressed as:

$$h \approx Cx^{0.5} \tag{4.1}$$

where x is the downwind distance from the leading edge of the continuous fuel bed and C is a coefficient. The values for coefficient C are 0.175 and 0.2 for I-4 and I-75 Superfog events, respectively. Using 4.1 one can forecast growth of the Superfog layer with distance over the fuel bed. In cases where the growth of the Superfog is observed to be 1 meter high over 30 meters of fuel, the constant C should be taken to be approximately 0.18. In cases where Superfog grows to 0.5 meters over 30 meters of fuel the constant C should be taken to be approximately 0.09. For cases where Superfog does not grow above 0.5 m high over 30 m of the fuel bed, Superfog is not likely to form.

Table 4.1. Model Inputs

Model Input	**Value**
Vapor flux	1.6 x 10^{-3} g m^{-2} s^{-1}
Heat flux	1.0 W m^{-2}
Friction velocity	0.1 m s^{-1}
Monin-Obukhov Length	100 m
Roughness height	0.01 m
Surface Temperature	1.66 ^{o}C (Gainesville 2012) 20 ^{o}C (I-4 2008)
Vertical Temperature Gradient	3 ^{o}C km^{-1}
Ambient Relative Humidity	60% (Gainesville 2012) 95 % (I-4 2008)

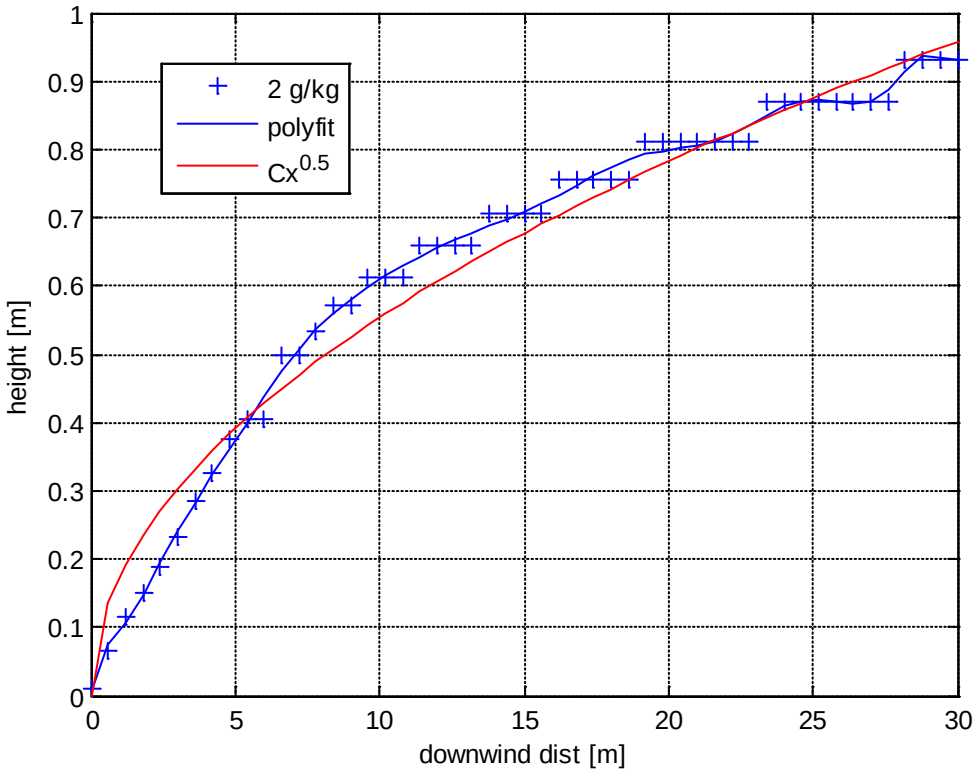

Figure 3.33. Boundary layer model prediction of growth of Superfog using weather conditions surrounding the I-4 disaster in 2008. Superfog defined to be anywhere where liquid water contents are greater than 2.0 g kg^{-1}. Over the course of 30m Superfog grows to a height of 1 meter. The height of Superfog will continue to grow. Here C=0.175.

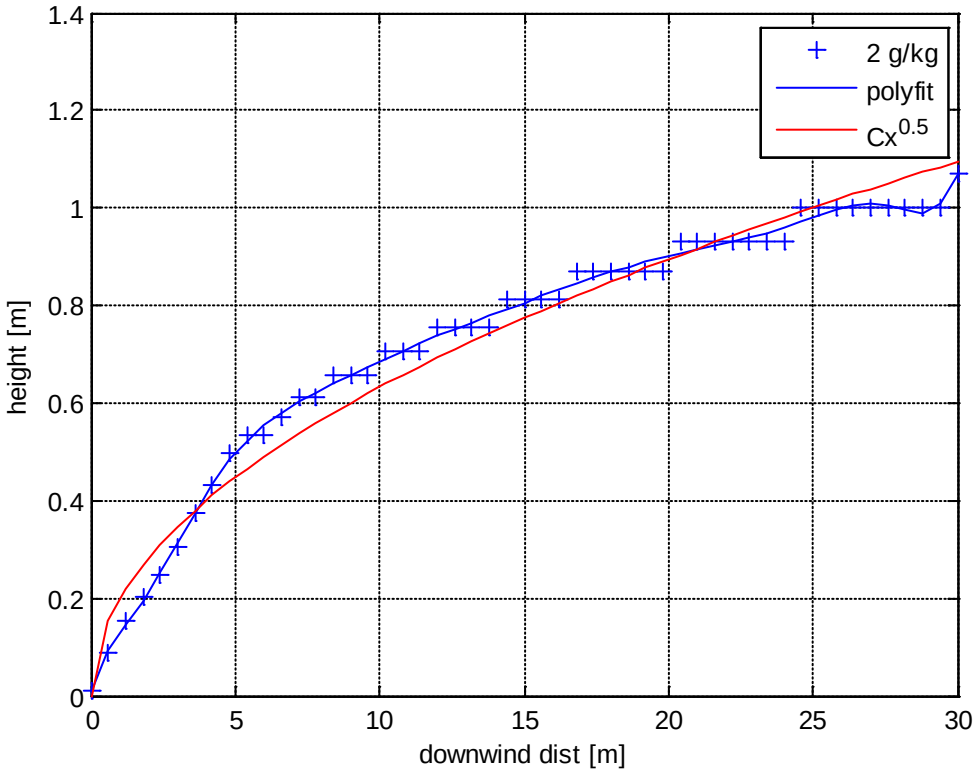

Figure 3.34. Boundary layer model prediction of growth of Superfog using weather conditions surrounding the morning of the Gainesville incident in 2012. Superfog defined to be anywhere where liquid water contents are greater than 2.0 g kg^{-1}. Over the course of 30m Superfog grows to a height of 1 meter. The height of Superfog will continue to grow with distance. Here C=0.2.

5. Conclusion

This project consisted of:

1. Theoretical Investigation of parameters relevant to Superfog formation
2. Numerical Analysis
    a. Thermodynamic Condensation
    b. Droplet size distribution, liquid water content, and visibility relations
    c. Boundary layer development
3. Experimental Investigation
    a. Smoke Measurements
    b. Superfog Formation
    c. Smoke Boundary Layer Growth

Though these activities the following was clarified to the certain extent:

1. Thermodynamic aspects of Superfog

2. Light scattering physics of fog droplets
3. Size distribution and number concentrations of fog droplets
4. Relations between fog droplet size and concentration to liquid water content and visibility
5. Necessary *lwc* and droplet concentrations to form Superfog
6. Boundary layer growth of Superfog
7. Smoldering heat and vapor flux
8. Smoke and ambient temperature, humidity, and visibility
9. Fuel moisture content impact on vapor production

We have attained a greater understanding of Superfog and the physics associated with its production. We have investigated numerical and physical models and experiments to understand the formation of extremely low visibility smoke that in extreme becomes Superfog.

We made radical modifications to the wind tunnel for climate control capabilities and have recreated historical Superfog events. We have produced a 2D boundary layer model which is validated by laboratory experiments and is capable of predicting historical Superfog events.

Thermodynamic modeling has allowed us to estimate fog formation or the lack of fog formation through mixing air masses with varying moisture contents. Using the Thermodynamic modeling we were able to determine realistic *lwc* values (2 g kg^{-1}) available from smoldering smoke to produce superfog. We have done sensitivity studying of the relations of liquid water content, droplet size distribution and visibility. Droplets with diameters similar to the wavelengths of visible light have reduced visibility twice as effectively compared to larger size droplets. Given *lwc* available is 2 g kg^{-1}, then droplets need to have radius of 1μm or smaller to be able to create Superfog visibility. Droplet distributions with geometric standard deviations greater than 1.3 lead to the inclusion of large droplets decreasing the efficiency of the volume of water to interrupt light. Droplet concentrations of 10^5 cm^{-3} are required to form Superfog. Literature suggests there is always sufficient CCN produced from biomass burning to produce this concentration.

Numerical, 2D boundary layer model has been formulated and includes thermodynamic processes to condense water vapor to form fog. Experiments were conducted to measure key parameters associated with smoldering smokes. Controlled Superfog Experiments showed the ability to form superfog in the wind tunnel under various temperature, humidity and *fmc* combinations. Superfog in these experiments have appeared when ambient temperatures are less than 40^oF, humidity over 80%, and *fmc* values of 40% or greater. It has been shown through experiments that the *fmc* plays a crucial role in the quality of superfog produced. The fuel moisture content allows more water vapor to be included into the smoke from combustion and vaporization. Boundary layer growth predictions made by 2D model were verified with experiments. The model can predict historic superfog events on the I-4 in 2008 and the I-75 in 2012. The model can be used to predict possibility of superfog events in future.

Table 5.1. Summary of Parameters Likely to produce Superfog

Parameter	Superfog Conditions
Droplet size	< 1 μm
CCN concentration	10^5 # cm^{-3}
lwc	>2 g kg^{-1}
Ambient temperature	<40°F (4.44°C)
Ambient Relative humidity	>80%
fmc	>40%
Wind velocity	<1 m s^{-1}

5.1. Recommendations for possible unknown Superfog prediction tool inputs

Land managers may not have all the parameters needed to run the newly developed Superfog prediction tool. This section gives some recommendations for approximations that can be used in the Superfog prediction tool when the actual measurements are absent.

Most commonly the vapor flux will need to be approximated. Vapor flux is produced from combustion reaction, vaporization from live and dead fuels and from soil. Dense fuels such as tree stumps and bushes can have vapor fluxes of 1.5 g m^{-2} s^{-1}. Packed pine needles and tree litters have vapor fluxes of 0.5 g m^{-2} s^{-1}. Open grass can produce vapor flux approximately 0.1 g m^{-2} s^{-1}. These suggestions should be doubled for fuel moisture contents over 40% or fuel is on moist ground.

Unless a tower with temperature measurements at different heights is located close to the site the temperature gradients will have to be approximated. Based on literature and our experience, during stable nighttime hours reasonable vertical temperature gradients are near 3°K per kilometer.

The friction velocity is a measure of the shear stress. Unless a sonic anemometer flux measurements or velocity measurements at different heights are available the friction velocity can be approximated to be 10% of the mean wind velocity.

The Obukhov Length characterizes the atmospheric stability. Common values to use for nighttime stable conditions are 100 meters. For extremely stable conditions 20 m can be used (very cold nights with no winds). For less stable conditions values of 1000 meters can be used (warm cloudy nights with some wind).

The roughness length characterizes surface conditions affecting the wind velocity profile near the surface. It is based on the fuels and obstacles in the burn area. In a forest area the roughness

length should be taken to be 1 meter. For low crops and bushes, roughness lengths should be taken to be 0.25 meters. For open terrain with mostly grass 0.03 meters is suggested.

Although the above recommendations are acceptable, more precise formulations for model inputs based on readily available measurements are needed. The model input recommendations are summarized in table 5.1.

Instructions for model use are given in Appendix B.

Table 5.2. Recommended Superfog software inputs

Model input parameter	Description	Recommended values if unavailable
Heat Flux [W m^{-2}]	Heat produce by smoldering fuel bed	1 W m^{-2}
Water Vapor Flux [g m^{-2} s^{-1}]	Water vapor produced from smoldering fuel bed	1.5 [heavy loading (thick bushes)] 0.5 [moderate fuel loading (grass and tree litters)] .1 [light fuel loading (grass)] * Double values if *fmc*>40% or on moist ground
Surface temperature [^{o}K]	Ambient ground level temperature	274-350 ^{o}K
Temperature Gradient [^{o}K m^{-1}]	Temperature changes of stable ambient atmosphere with height	$3x10^{-3}$ ^{o}K m^{-1}
Ambient Humidity [%]	Ambient relative humidity	50-95%
Friction velocity [m s^{-1}]	Shear velocity	10% of current wind speed
Obukhov Length [m]	Atmospheric Stability	20 m [cold & low wind velocity] 100 m 1000 m [warm & cloudy night]
Roughness length [m]	Roughness height based on fuel bed height	1 m [forest] 0.25m [low crops] .03m [open flat terrain mostly grass]

6. References

Achtemeier G.L. 2001. Simulating nocturnal smoke movement. Fire Management Today. 61: 28–33.

Achtemeier, Gary L., 2003. On the Origins of "Superfog" – A Combination of Smoke and Water Vapor that Produces Zero Visibility over Roadways. In: Proceedings 2nd international wildland fire ecology and fire management congress and 5th symposium on fire and forest meteorology. J8.9. Boston: American Meteorological Society: 1—4.

Achtemeier, G.L. 2008. Effects of moisture released during forest burning on fog formation and implications for visibility. Journal of Applied Meteorology and Climatology. 47: 1287–1296.

Achtemeier, G.L. 2009. On the formation of superfog in woodland smoke. Meteorological Applications. 16: 215–225.

Asa-Awuku, A., Engelhart, G. J., Lee, B. H., Pandis, S. N., Nenes, A. 2009. Telating CCN activity, volatility, and droplet growth kinetics of Beta-caryophyllene secondary organic aerosol. Atmos. Chem. Phys., 9, 7695-812

Cimorelli, A., Perry, S., Venkatram, A., Weil, J., Paine, R., Wilson, R., Lee, R., Peters, W., Brode, R., 2005. AERMOD: a dispersion model for industrial source applications. Part I: general

Eagan. (1974). Measurements of Cloud Condensation Nuclei and Cloud Droplet Size Distributions in the Vicinity of Forest Fires forest fires. AMS Online Journals. AMS Online Journals.

Fišák, J., Řezáčová, D., & Mattanen, J. (2006). Calculated and measured values of liquid water content in clean and polluted environments. Studia Geophysica et Geodaetica, 50(1), 121-130.

Fuzzi, S., Facchini, M. C., Decesari, S., Matta, E., & Mircea, M. (2002). Soluble organic compounds in fog and cloud droplets : what have we learned over the past few years ? Atmospheric Research, 64, 89 - 98.

Holle, R. (1971). Effects of cloud condensation nuclei due to fires and surface sources during South Florida droughts. Journal of Applied Meteorology, 10(1), 62–69.

Lowe, Paul R., 1977: An Approximating Polynomial for the Computation of Saturation Vapor Pressure. *J. Appl. Meteor.*, 16, 100–103.

Nebuloni, R. 2005. Empirical relationships between extinction coefficient and visibility in fog. Applied Optics. Vol. 44, No. 18 / 20

Parmar, R.S., Welling, M., Andreae, M.O., Helas, G., 2008. Water vapor release from biomass combustion, Atmos. Chem. Phys., 8, 6147-6153.

Podzimek, J. 1997. Droplet Concentration and Size Distribution in Haze and Fog. Studia Geophysica et Geodaetica. Vol. 41, issue 3, pp 277-296.

model formulation and boundary layer characterization. *Journal of Applied Meteorology* 44, 682-693.

Tang, I.N. 1996. Chemical and size effects of hygroscopic aerosols on light scattering coefficients. J. of Geophysical Reasearch, Vol. 101, No. D14, p19245-19250.

Ward, T., Hamiltonjr, R., Dixon, R., Paulsen, M., & Simpson, C. (2006). Characterization and evaluation of smoke tracers in PM: Results from the 2003 Montana wildfire season. Atmospheric Environment, 40(36), 7005-7017. doi: 10.1016/j.atmosenv.2006.06.034.

APPENDIX A

Fire Lab Wind Tunnel

Contents

Table of Figures

System Start Up

Note: Steps 1-4 need to be completed at least one hour prior to the start of testing.

Step 1: Turn Breakers on in the electrical panel (Main, Chiller & Pump, Control Circuit, and Humidifier). See Figure 1.

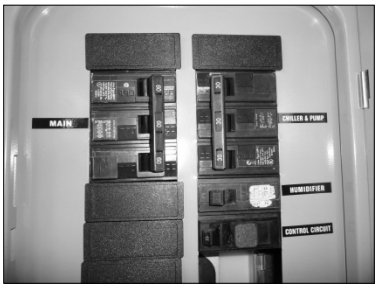

Figure 1. Electrical Panel

Step 2: Push green "Run" button on pump controller inside control panel. See Figure 2.

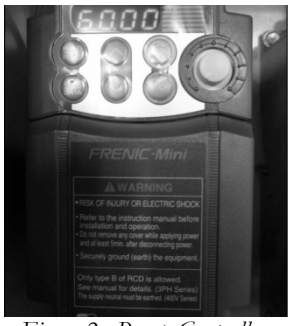

Figure 2. Pump Controller.

Step 3: Make sure that the pump discharge valve to the chiller coil is set to the proper position, and that the temperature controller is set for at least 40 °F. See Figures 3 and 4.

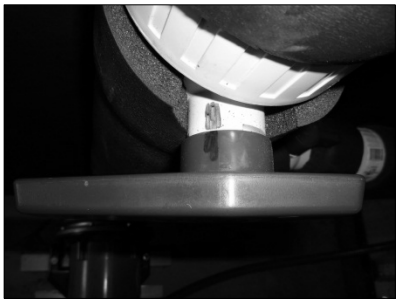

Figure 3. Pump Discharge Valve.

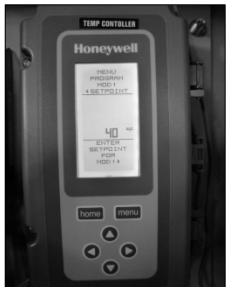

Figure 4. Temperature Controller.

Step 4: Hold the chiller ON/OFF button until the chiller turns ON. See Figure 5.

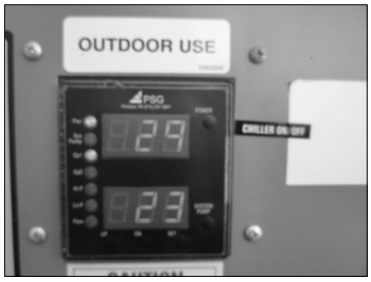

Figure 5. Chiller ON/OFF Button.

Step 5: Hook water hose to water spigot. Purge all the air out of hose, then hook hose to Humidifier Filter, connected to the water filter, using the quick disconnect fitting. Turn water on. See Figures 6 and 7.

Figure 6. Humidifier Filter (left), Spigot (center), and Water Heater (right).

Step 6: Once chiller has cycled off and the humidifier is up to temperature, the system can be set for a test condition.

Step 7: Set Temperature Controller for desired temperature. See Figure 4.

Step 8: Turn chiller off. Press and hold the ON/OFF button until chiller turns off. See Figure 5.

Step 9: Open large main line valve to chiller coils and close small valve to outside chiller unit. See Figure 7 for valve positions.

Figure 7. Discharge Valves in Test Operating Positions.

Step 10: Plug in fan controller and set fan to frequency (in Hz) corresponding to desired wind speed (in meters per second). Do not turn fan on. See Figure 8.

Figure 8. Fan Controller.

Step 11: Set humidifier set point to 80% RH. Turn on humidifier control switch. Turn on humidifier purge switch for 10 seconds. Look for steam at purge point. Turn off purge switch and control switch. Set humidity controller to desired humidity.

Figure 9. Humidifier Control Switch (left), Humidifier Control (center), and Humidifier Purge Switch (right).

Step 12: Start Fan by pressing "Run" button on fan controller. See Figure 8.

Step 13: Turn on humidifier control switch. See Figure 9.

Step 14: Monitor ambient temperature and relative humidity in wind tunnel via temperature controller and humidifier control seen in Figures 4 and 9, respectively. Once desired conditions are achieved, set fire in a safe manner.

Run test for as long as desired conditions are maintained by system. System should hold set for at least five minutes, maybe longer, depending on outside weather conditions.

Procedure for Re-Testing

Step 1: At the completion of a test, shut off humidifier control switch and fan controller.

Step 2: Open discharge valve to chiller and set the discharge valve to the evaporator coils to the marked position. See Figure 10.

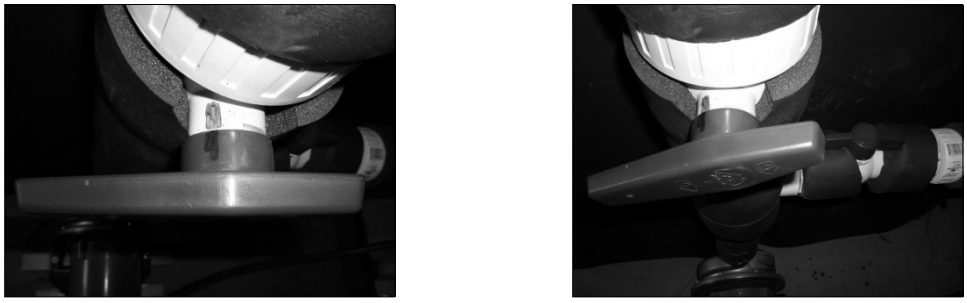

Figure 10. Discharge Valve to Chiller Coils (left) and Discharge Valve to Chiller (right).

Step 3: Set temperature controller to 40 °F.

Step 4: Turn chiller ON.

Step 5: Wait until chiller cycles off. This may take 20-60 minutes, depending on outside weather conditions.

Step 6: Repeat Steps 6-14 from previous section to complete another test.

Shutdown Procedures Following Test Completion

Step 1: Shut off humidifier control switch and fan controller.

Step 2: Shut off pump controller by pushing the red "STOP" button. See Figure 2.

Step 3: Flip breakers in the power panel to OFF position (Chiller/Pump, Control Circuit, and Humidifer).

Step 4: Shut off water to humidifier and disconnect hose from humidifier and from spigot. Store hose in pan next to humidifier.

Successful completion of these steps will result in full system shutdown.

Contact Information

For any procedural or service related questions, please call:

Gary Long at (909) 821-6359
A+ Air Corp.

APPENDIX B

Superfog Analysis Model - SAM

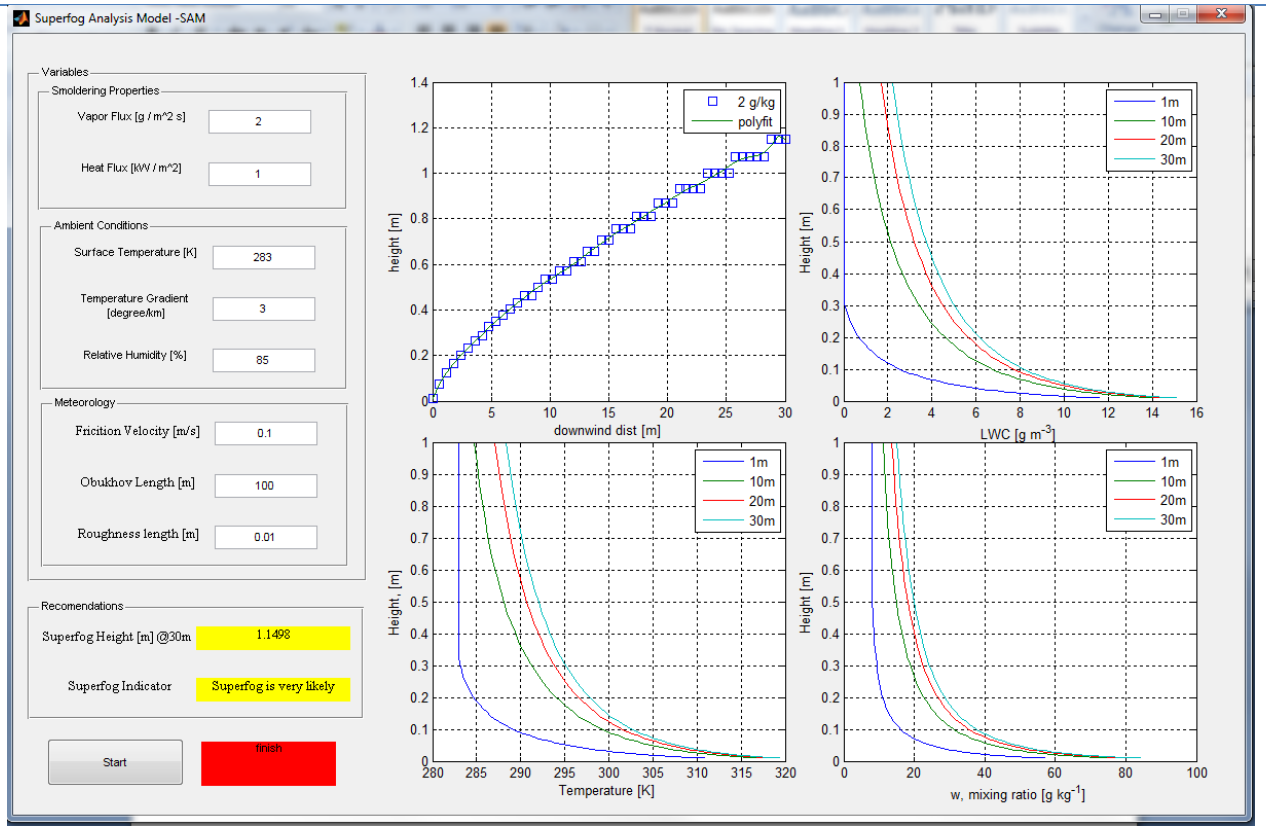

Contents

List of Tables

List of Figures

1. System Requirements

The Superfog Analysis Tool requires a workstation with MATLAB package.

2. Installation

2.1 First Time Running the Superfog Analysis Tool

First run MATLAB on your machine. An example of the MATLAB home screen is shown in Figure 1.

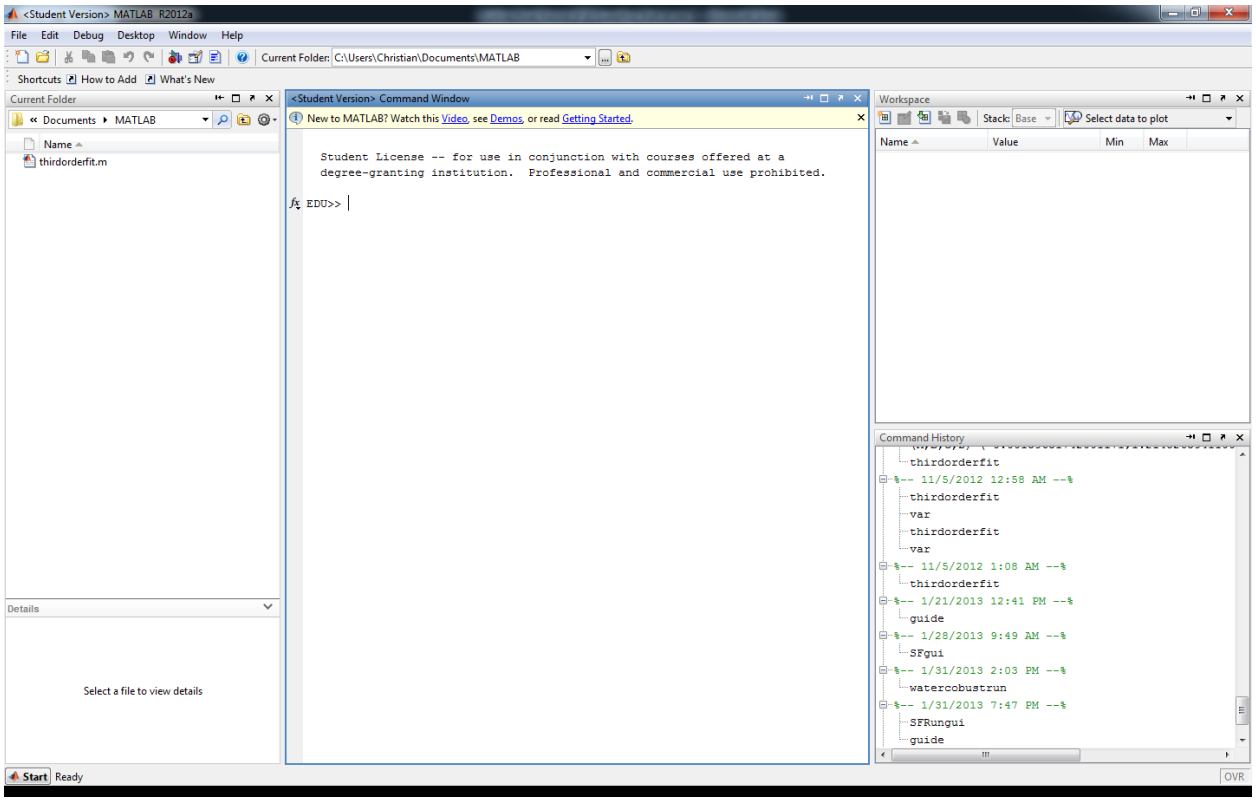

Figure 1. MATLAB home screen

In the command window, we will run “guide” (Figure 2).

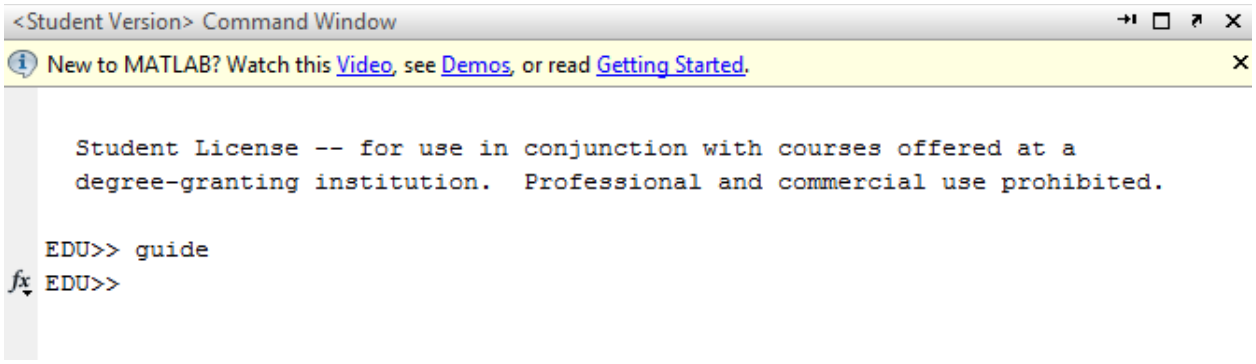

Figure 2. Run “guide” in the Command Window

This will open the MATLAB GUI quick start (Figure 3). Go to the “Open Existing GUI” tab. Click on “Browse…” to locate the directory containing the Superfog Analysis Tool. Then open the SFRungui.fig.

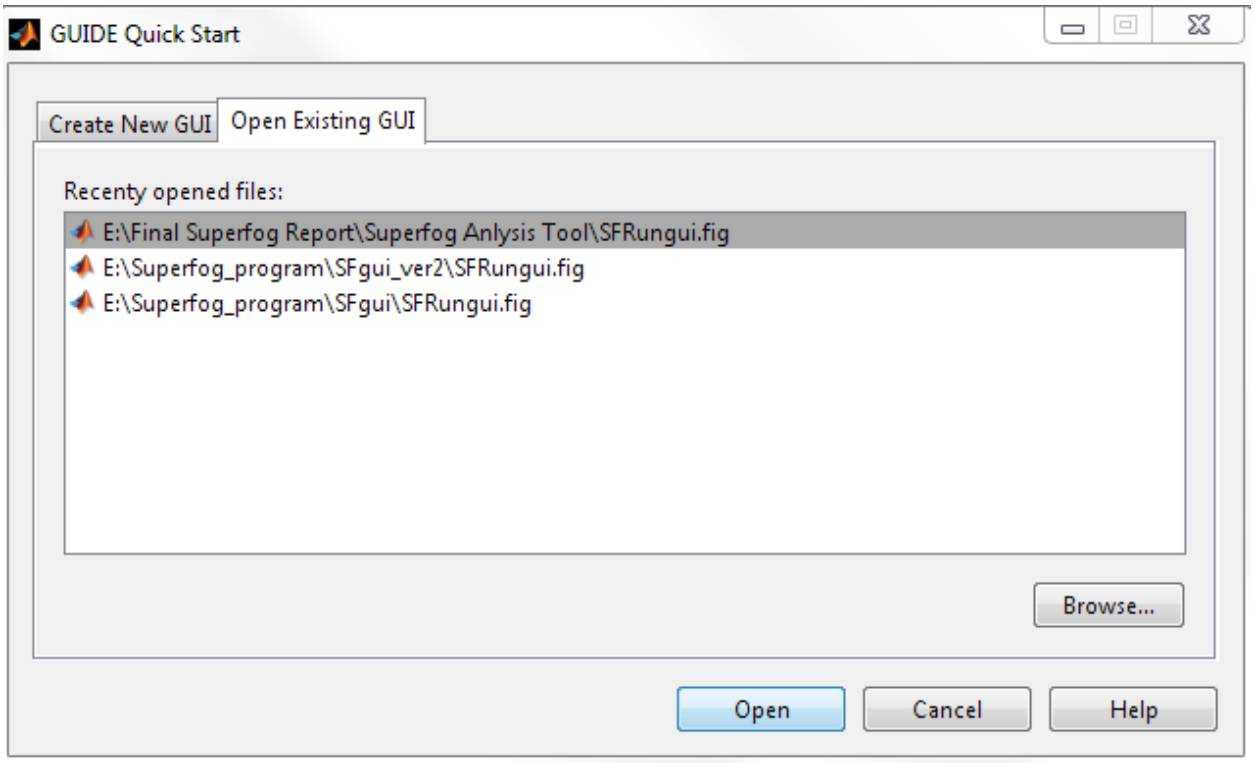

Figure 3. Selecting the file location of SFRungui.fig file

This will open the MATLAB GUI for the SAM. Note: This screen will not run simulations of the SAM software. The next step is to press the play button highlighted in Figure 4 which activates the SAM software (Figure 5).

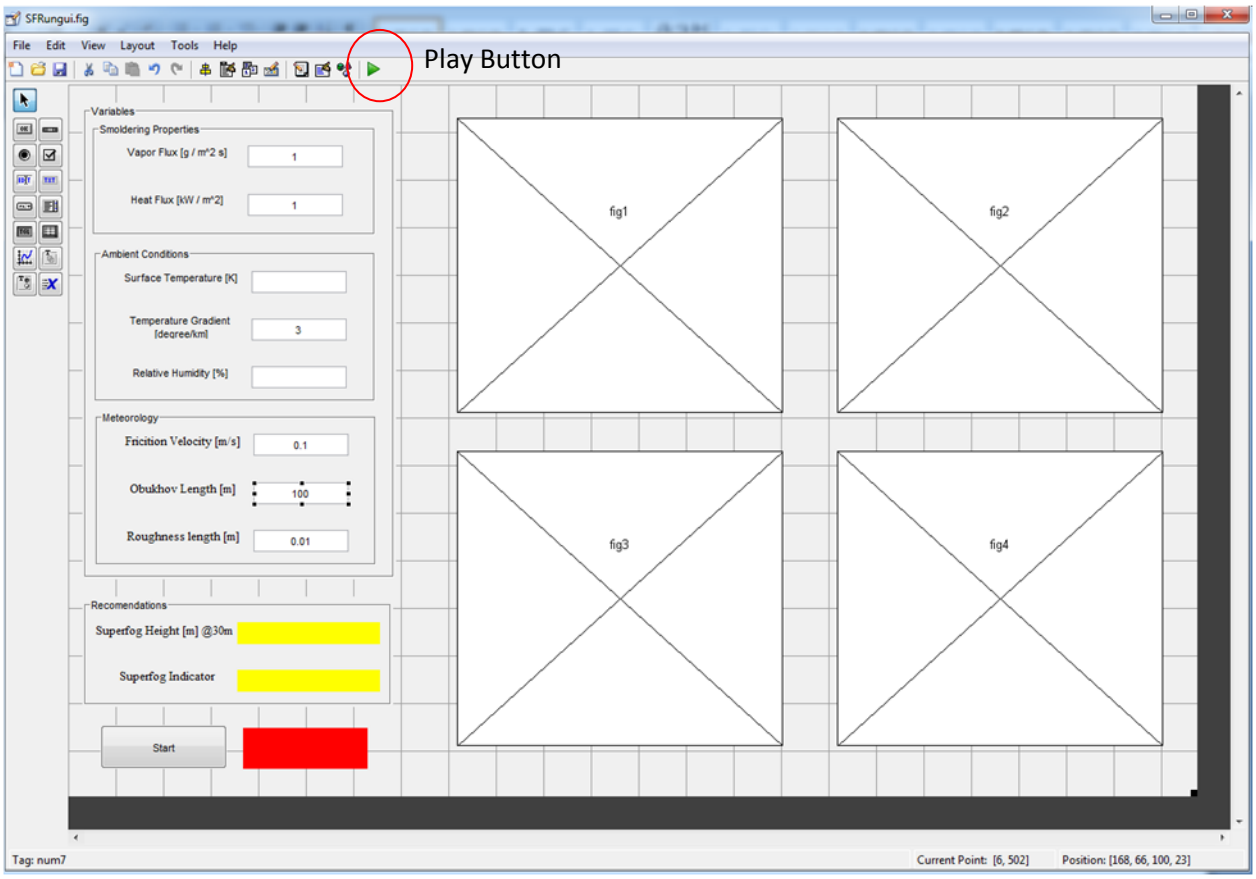

Figure 4. MATLAB GUI creation screen with the play button circled in red.

This concludes the first time installation of the SAM. In future uses of this application, "SFRungui" may be run from the command window. The "Current Folder" on the home screen must be in the same directory where the SFRungui is located.

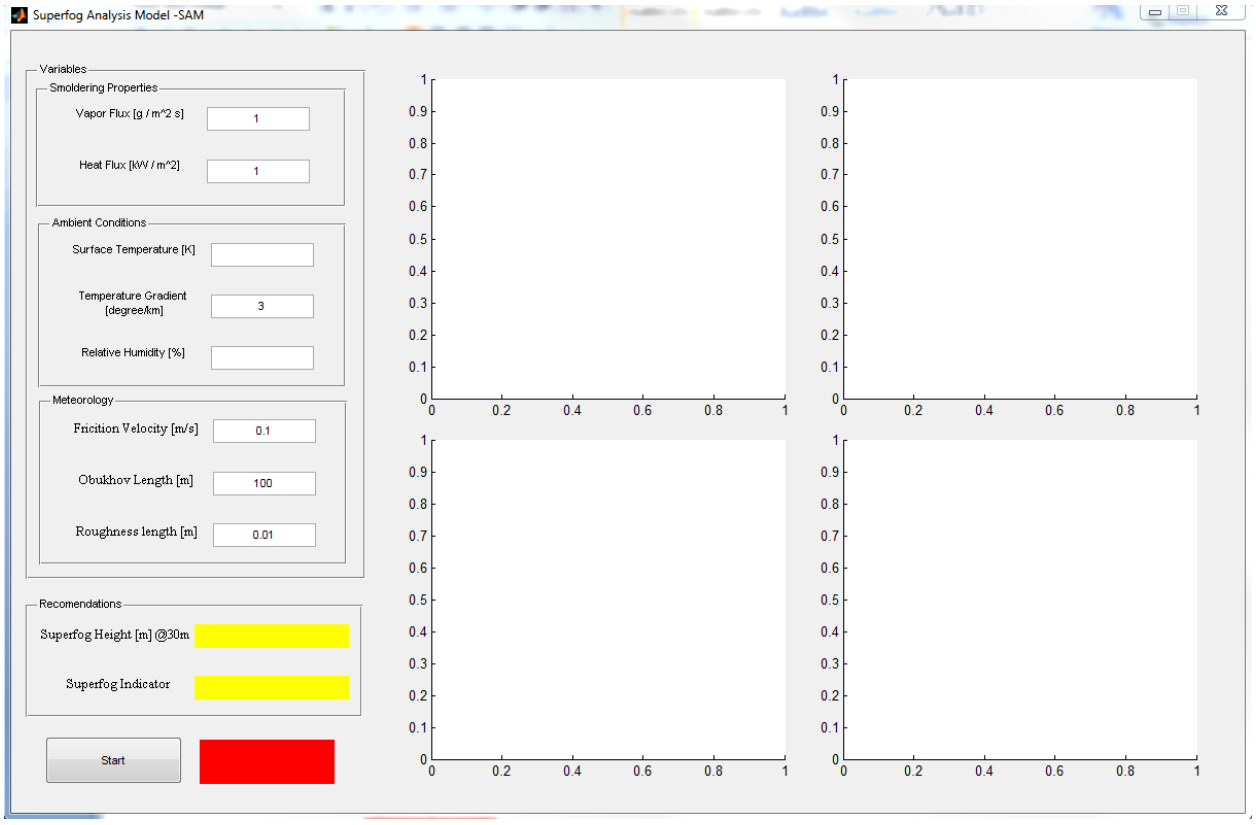

Figure 5. Superfog Analysis Model workspace

3. SAM Input Variables

The SAM has 3 major categories of input variables: Smoldering Properties, Ambient Conditions, and Surface Meteorology. The input variables include: vapor flux, heat flux, surface temperature, relative humidity, friction velocity, Obukhov length, and surface roughness. The editable variables can be changed in the white text boxes next to variable descriptions. This section will describe the variable inputs and suggestions if inputs are unknown.

Although the recommendations given in the following part are acceptable, more precise values for model inputs based on readily available measurements should be used whenever available. The model input recommendations are summarized in Table 1. After variables are chosen click on the "Start" button on the SAM.

3.1 Water Vapor Flux

Most commonly the vapor flux will need to be approximated. Vapor flux is produced from combustion reaction, vaporization from live and dead fuels and from soil. Dense fuels such as tree stumps and bushes can have vapor fluxes of 1.5 g m^{-2} s^{-1}. Packed pine needles and tree litters have vapor fluxes of 0.5 g m^{-2} s^{-1}. Open grass can produce vapor flux approximately 0.1 g

m^{-2} s^{-1}. These suggestions should be doubled for fuel moisture contents over 40% or fuel is on moist ground.

3.2 Heat Flux

Heat flux measurements have been made for smoldering fuels at the USDA Forest Service PSW Research Station in Riverside, CA. Measurements from Huskeflux RC01 sensor indicate smoldering fuels produce up to 1 kW m^{-2}.

3.3 Surface Temperature

The surface temperature of the site may be taken from local weather station or any temperature measurements readily available.

3.4 Temperature Gradient

Unless a tower with temperature measurements at different heights is located close to the site the temperature gradients will have to be approximated. Based on literature and our experience, during stable nighttime hours reasonable vertical temperature gradients are near 3^{o}K per kilometer.

3.5 Relative Humidity

Humidity measurements from local weather station or airport are ideal. In the absence of measurements one can use values between 60-80% based on familiarity with local seasonal conditions.

3.6 Friction Velocity

The friction velocity is a measure of the shear stress. Unless a sonic anemometer flux measurements or velocity measurements at different heights are available the friction velocity can be approximated to be 10% of the mean wind velocity. For wind speeds less than 1 m/s, friction velocity is suggested to be 0.1 m/s.

3.7 Obukhov Length

The Obukhov Length characterizes the atmospheric stability. Common values to use for nighttime stable conditions are 100 meters. For extremely stable conditions 20 m can be used (very cold nights with no winds). For less stable conditions values of 1000 meters can be used (warm cloudy nights with some wind).

3.8 Roughness Length

The roughness length characterizes surface conditions affecting the wind velocity profile near the surface. It is based on the fuels and obstacles in the burn area. In a forest area the roughness

length should be taken to be 1 meter. For low crops and bushes, roughness lengths should be taken to be 0.25 meters. For open terrain with mostly grass 0.03 meters is suggested.

Table 1. Recommended Superfog model inputs

Model input parameter	Description	Recommended values if unavailable
Heat Flux [W m^{-2}]	Heat produce by smoldering fuel bed	1 kW m^{-2}
Water Vapor Flux [g m^{-2} s^{-1}]	Water vapor produced from smoldering fuel bed	1.5 [heavy loading (thick bushes)] 0.5 [moderate fuel loading (grass and tree litters)] .1 [light fuel loading (grass)] * Double values if *fmc* > 40% or on moist ground
Surface temperature [^oK]	Ambient ground level temperature	274-350 ^oK
Temperature Gradient [^oK m^{-1}]	Temperature changes of stable ambient atmosphere with height	$3x10^{-3}$ ^oK m^{-1}
Ambient Humidity [%]	Ambient relative humidity	50-95%
Friction velocity [m s^{-1}]	Shear velocity	10% of current wind speed or 0.1 m s^{-1} for wind velocities less than 1 m s^{-1}
Obukhov Length [m]	Atmospheric Stability	20 m [cold & low wind velocity] 100 m 1000 m [warm & cloudy night]
Roughness length [m]	Roughness height based on fuel bed height	1 m [forest] 0.25m [low crops] .03m [open flat terrain mostly grass]

4. Prediction Tool Outputs and Recommendations

After pressing the "Start" button, program execute all simulation modules. The simulation can take up to 1 minute of time. When the simulation is complete: "finish" will appear in the red area, 4 plots will be generated, and recommendation fields in yellow will be filled. The SAM plots 4 graphs to better understand the formation or the failure to form Superfog. The first figure (top left) plots the growth in height of the Superfog layer over the downwind distance of the fuel bed. An example plot is given in Figure 6. The blue squares indicate the data points calculated by numerical simulations and the green line indicates a smooth polynomial fit of data. The second plot (top right) shows model results for the *LWC* vertical profiles at four downwind distances from the leading edge of the fuel bed (Figure 7). The third plot (bottom left) shows model results for vertical temperature profiles at four downwind distances from the leading edge of the fuel bed (Figure 8). The last plot (bottom right) indicates the vertical profiles of mixing ratio for four downwind distances from the leading edge of the fuel bed (Figure 9).

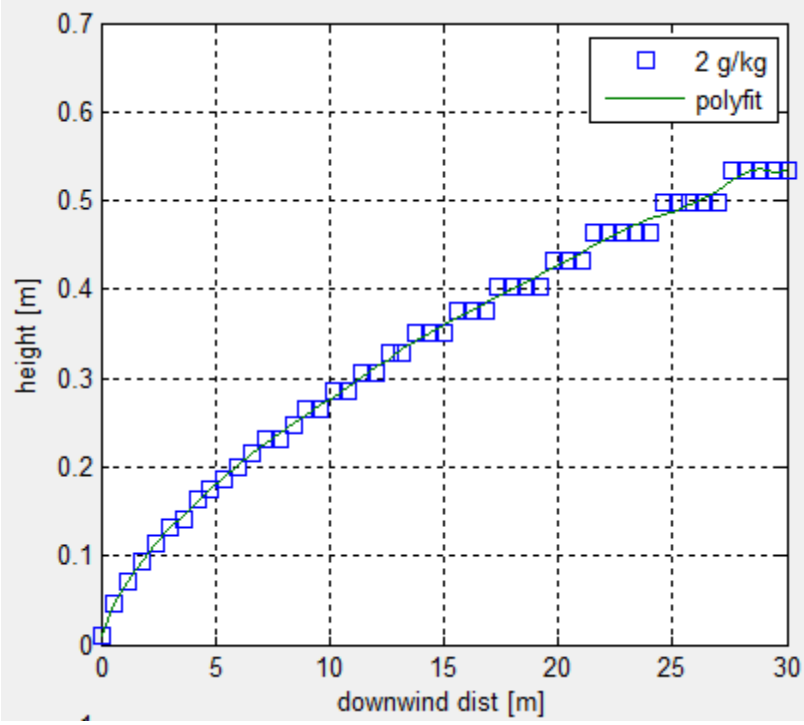

Figure 6. Growth of Superfog with the distance from the upwind edge of the fire.

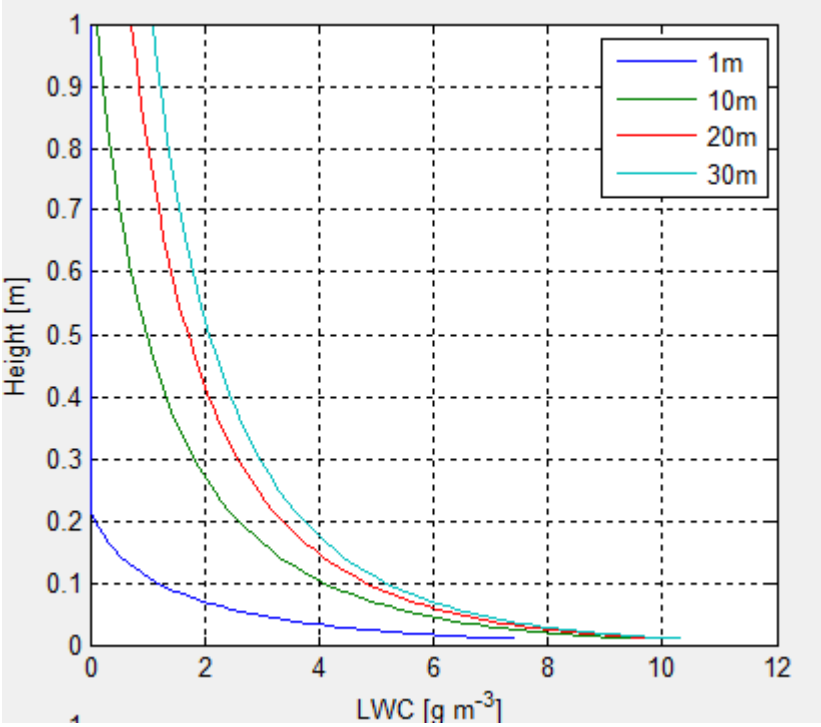

Figure 7. Vertical Profiles of *LWC* at four distances from the upwind edge of the fire.

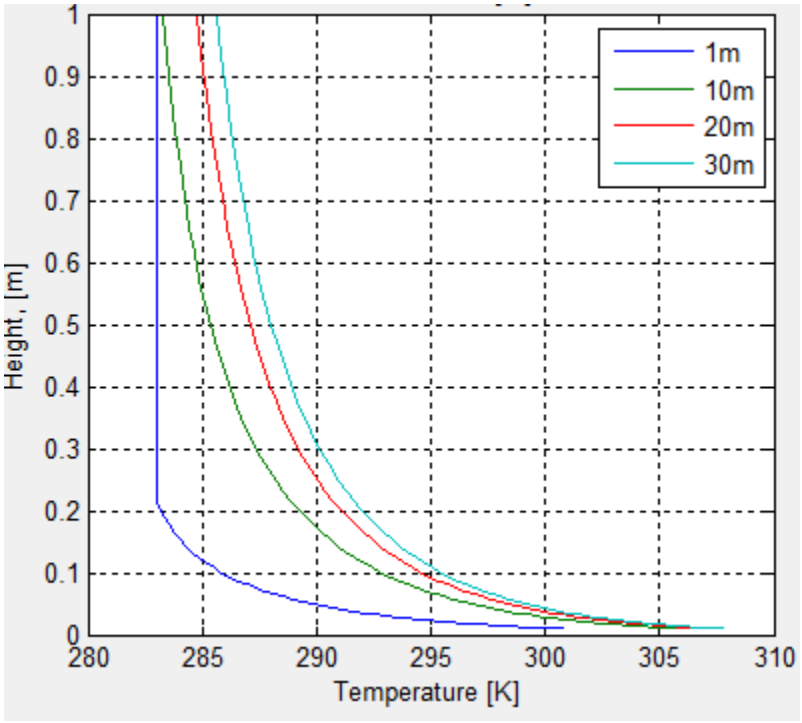

Figure 8. Vertical Temperature Profiles at four distances from the upwind edge of the fire..

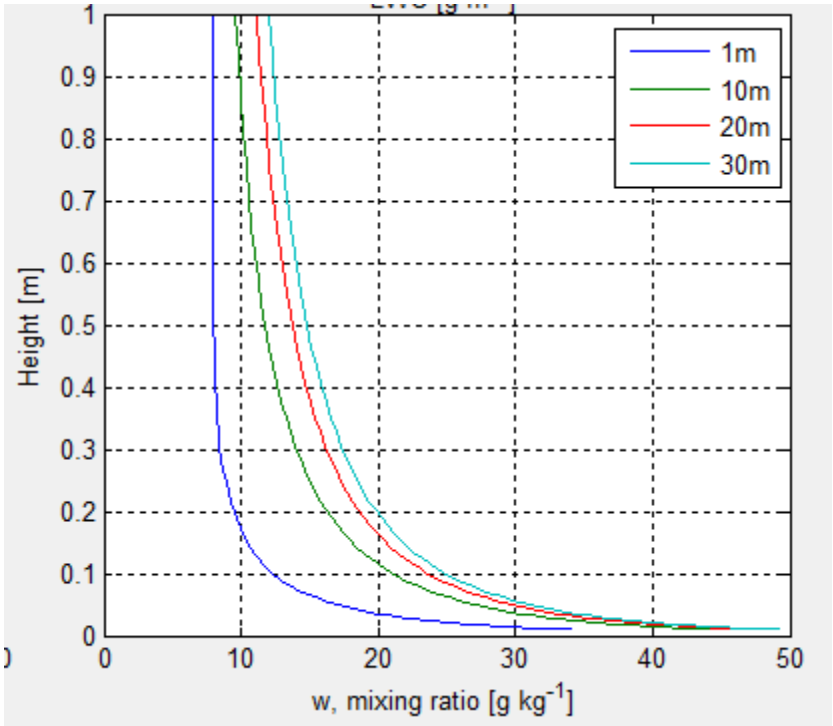

Figure 9. Vertical Profiles of the mixing ratio at four distances from the upwind edge of the fire.

The Recommendation section of the SAM displays the height of the Superfog at 30 meters into fuel bed. Based on the height reached at this point recommendation of likelihood of Superfog formation is expressed in the "Superfog Indicator" section. Table 2 summarizes likeliness of Superfog and growth of Superfog.

Table 2. Possible Superfog Indicator Recommendations

Superfog Indicator	**Superfog Height at 30m into the fuel bed (*h*)**
Superfog is very likely	1 m < *h*
Superfog is possible	0.5 m < *h* < 1.0 m
Superfog is not likely	0.1 m < *h* < 0.5 m
Zero Superfog threat	*h* < 0.1 m